Surface Properties of Double-Fin Generated Shock-Wave/Boundary-Layer Interactions

Seckin, Serdar
Mears, Lee J.
Song, Myungjun
Alvi, Farrukh S.
Zigunov, Fernando

To be published in: AIAA Journal

DOI to publisher's version: 10.2514/1.J062886

Surface Properties of Double-Fin Generated Shock-Wave/Boundary-Layer Interactions

Serdar Seçkin *, Lee J. Mears †, MyungJun Song ‡, and Farrukh S. Alvi §
FAMU-FSU College of Engineering, Florida Center for Advanced Aero-Propulsion (FCAAP), Florida State University, Tallahassee, Florida, 32310

Fernando Zigunov ¶
Los Alamos National Laboratory, Los Alamos, New Mexico, 87545

Shock-Wave/Boundary-Layer Interaction (SBLI) is ubiquitous in high-speed air vehicles. SBLI surface flowfield properties of crossing shocks induced by symmetric Double-Fins (DF) at fin angles of 8° and 10° at Mach 2 are experimentally investigated; a 10° Single-Fin (SF) is also explored as a comparison. Surface visualization is used to capture distinct flowfield structures such as separation and upstream influence. Steady and unsteady Pressure-Sensitive Paint (PSP) are used to obtain global surface pressure fields. Characteristics of DF-SBLI surface topology are discussed by comparing the corresponding SF-SBLI. The effect of fin angle on DF-SBLI is characterized, and unsteady dynamics of the pressure field are examined. Spectral Proper Orthogonal Decomposition (SPOD) is performed on unsteady PSP, and traveling surface pressure waves and their frequency dependent behavior are discussed. Dispersion relation of surface pressure waves is revealed by performing 2-D space-time Fourier transform on unsteady PSP, and the results are compared with the phase velocity distributions obtained from SPOD. Accompanying group velocity behavior is examined for distinct SBLI regions wherein wave propagation is found dependent on its frequency. Steady surface pressures along the centerline are compared with previous experimental data. Fin-tip-spacing is found to be an essential parameter for scaling of upstream influence length.

Nomenclature

f = Frequency

G_{xx}, G_{yy} = Autospectral density function

This paper builds upon the knowledge gained from the study that was presented as paper at the AIAA Scitech 2022 forum wherein the accompanying video presentation is also available [1].

*Graduate Research Assistant, Department of Mechanical Engineering, serdar.seckin@fsu.edu, AIAA Student Member
†Graduate Research Assistant, Department of Mechanical Engineering, AIAA Student Member
‡Graduate Research Assistant, Department of Mechanical Engineering, AIAA Student Member
§Professor, Department of Mechanical Engineering, AIAA Associate Fellow
¶Postdoctoral Researcher, Physics Division, AIAA Member

G_{xy} = Cross-spectral density function

H = Fin height

I = Light intensity count

k = Wavenumber, $k = 2\pi/\lambda$

L = Fin length

m = SPOD mode number

M_∞ = Freestream Mach number

M_n = Normal Mach number, $M_n = M_\infty \sin\beta$

P = Absolute static surface pressure

$\overline{P}$ = Time-averaged surface pressure

P_∞ = Freestream surface pressure

St_δ = Strouhal number, $St_\delta = f\delta/U_\infty$

t = Time

T = Temperature

U_∞ = Freestream velocity

υ_{gr} = Group velocity, $\upsilon_{gr} = d\omega/dk = 2\pi df/dk$

υ_{ph} = Phase velocity, $\upsilon_{ph} = \omega/k = 2\pi f/k = \lambda f$

W = Fin-tip-spacing

α = Fin angle

β = Inviscid shock angle

δ = Boundary-layer thickness

γ_{xy} = Coherence function

λ = Wavelength, $\lambda = 2\pi/k$

λ_s = SPOD eigenvalue

μ = Mean

ρ_{xy} = Pearson correlation coefficient

σ = Standard deviation

θ = Phase angle, $\theta = \omega t = 2\pi f t$

DF = Double-Fin

PS = Primary Separation

PSD = Power Spectral Density

PSP = Pressure-Sensitive Paint

SF = Single-Fin

SPOD = Spectral Proper Orthogonal Decomposition

UI = Upstream Influence

I. Introduction

Shock-wave/boundary-layer interactions (SBLIs) are inescapable for an air vehicle operating at transonic, supersonic, and hypersonic speeds. SBLIs can be observed on control surfaces, compression ramps on engine inlets, wings operating at transonic conditions, and turbine blades [2]. They cause unsteady pressure loadings and high heat flux on surfaces of the vehicle which can lead to fatigue [3, 4]. If the interaction strength is large enough, localized adverse pressure gradients lead to flow separation which drastically changes the overall flowfield [5]. Therefore, understanding the flow physics of the interaction is important to design efficient and robust high-speed air vehicles.

The flow physics of SBLIs can be complex even in simple geometries. Thus, building proper canonical forms (i.e., basic simplified geometries) and understanding their flowfield characteristics are essential for applications where SBLI plays a role. Several canonical configurations have been suggested in previous studies and they can be classified into 2-D and 3-D SBLI [6]. Délery et al. [7] further classified the 2-D interactions into impinging shock reflections, compression ramps, forward facing steps and backward facing steps. Settles and Dolling [8] illustrated some of the basic configurations regarding 3-D swept interactions including sharp-fins, swept-compression-ramps, and swept-impinging-shocks. The present study focuses on SBLI generated by two sharp-fins, in other words Double-Fin, which is one of the most common 3-D swept interactions in engine inlets.

In fin-generated SBLI, a sharp-fin at an angle-of-attack is situated perpendicular onto a plate with an incoming boundary layer. The attached oblique shock initiated from the fin leading edge interacts with the incoming boundary layer on the plate, resulting in a Single-Fin (SF) interaction. SF SBLI has been extensively studied both experimentally and computationally [9–18]. Alvi [19] investigated SF SBLI flow features and showed that flowfield exhibits quasi-conical symmetry away from the inception region near the fin tip, wherein mean flow features are invariant along the rays of upstream influence, separation line, and inviscid shock wave. The extensions of these rays merge at a Virtual Conical Origin (VCO) [10, 13]. Consequently, SF SBLI exhibits a swept interaction and it is topologically classified as *open separation* since cross-flow dominates overall interaction [20]. Hence, the only relevant length scale for a semi-infinite interaction is the boundary-layer thickness and its effect is mostly confined to the inception region [21]. Detailed discussions on the scales of separation region and unsteadiness for strong swept SBLIs are well documented in Refs. [22–26].

Building upon the knowledge gained from SF studies, Double-Fin (DF) studies were conducted to investigate SBLI of crossing shocks. An illustration of a typical DF SBLI flow structure with separation is depicted in Fig. 1. SBLI near

the fin leading edges is identical to that of a SF interaction. However, as the interaction grows towards the inviscid shock crossing, the flowfield significantly differentiates from the SF SBLI. For instance, a section view perpendicular to the main flow stream shows how the λ-shocks above the separation vortex interact in the centerline wherein Primary Separation lines start to turn parallel to each other. Mee et al. [27] performed one of the early studies of crossing shocks where the interactions were relatively weak since no boundary-layer separation was observed. Batcho et al. [28] studied symmetric and asymmetric DF interactions at Mach 3 with fin angles ranging from 7° to 11°, and Poddar and Bogdonoff [29] investigated the fluctuating wall pressures for the same experimental set and found significant unsteadiness at the centerline of the interaction. Hingst and Williams [30] performed experiments with fin angles ranging from 4° to 12° at a range of Mach numbers from 2.5 to 4.0 and investigated the unstart limits wherein the fins span the tunnel test section. Garrison [21, 31–34] employed Planar Laser Scattering and skin friction measurements to reveal extensive global viscous effects and irregular Mach reflection near the shock crossing at Mach 4 with 15° fin angle. Gaitonde and Knight [15] were the first to simulate crossing shocks computationally at Mach 2.95 with fin angles 4° and 8° using Reynolds-averaged methods. More recently, Adler and Gaitonde [35] studied the unsteadiness of 15° DF interaction at Mach 4 computationally using time-resolved Large Eddy Simulations and showed there may exist a low-frequency unsteadiness at shock crossing. However, generalized length scales associated with DF interactions have not been fully determined to date, and the available data sets are limited and insufficient to understand the flow physics of such complex interactions.

In the present study, experimental investigation of a symmetric DF interaction with 8° and 10° fin angles at Mach 2 is performed to explore the effect of fin angle on DF SBLI. 10°SF case is also implemented to examine the similarities and differences between SF and DF flowfields since DF SBLI is a non-linear compound interaction of two SFs. Oil flow surface visualization is applied to obtain primary topological flow features, such as upstream influence (UI) and

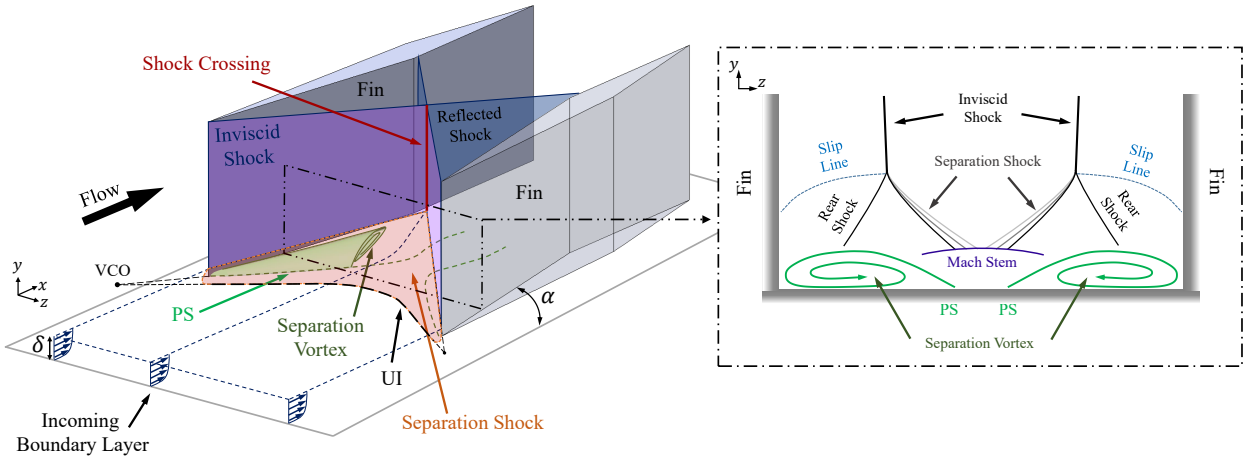

Fig. 1 Main flow features of the shock/boundary-layer interaction in the Double-Fin configuration (not to scale). VCO: Virtual Conical Origin, UI: Upstream Influence, PS: Primary Separation line. Supplementary graphical illustrations are available in the video presentation in Ref. [1].

primary separation (PS) [21]. Steady/unsteady Pressure-Sensitive Paint (PSP) measurements are performed to obtain global surface pressure and its unsteady characteristics. Spectral Proper Orthogonal Decomposition (SPOD) method is applied to the unsteady PSP data to understand dynamic characteristics of surface pressure field, and the existence of traveling surface pressure waves and their frequency dependent behavior are revealed. 2-D space-time Fourier transform is applied on the unsteady PSP data to obtain the dispersion relation of the surface pressure waves, and the comparisons with the phase velocity distributions computed from SPOD are explored to understand the underlying flow dynamics. Unlike SF SBLI, boundary-layer thickness is no longer the only characteristic length scale in DF interaction. To evaluate the scaling parameters in DF SBLI, centerline pressure measurements of 10°DF are compared to previous studies [21, 28], which have similar interaction strengths and incoming boundary-layer thicknesses, and based on this comparison, the role of fin-tip-spacing (W) as a scaling parameter is discussed.

II. Experimental Setup

A. Wind Tunnel Facility

Experiments are performed in the supersonic Pilot wind tunnel at the Florida Center for Advanced Aero-Propulsion (FCAAP) at FAMU-FSU College of Engineering. This is a blow-down facility which uses dry air fed at 3.45 MPa. The height and the width of the test section are 76.2 mm and 101.6 mm, respectively. Three sides of the test section are equipped with Schlieren-quality glass windows. The nominal freestream Mach number (M_∞) is 2 and the stagnation pressure (P_0) is 345±2 kPa and the stagnation temperature (T_0) is 293±5 K. Freestream velocity (U_∞) is 510±10 m/s and the freestream unit Reynolds number is 44×10^6 m^{-1}. The incoming boundary-layer thickness (δ) is estimated to be 3.5±0.2 mm, which is characterized by the previous study using Particle Image Velocimetry [36]. Additionally, the displacement thickness, momentum thickness, shape factor and the skin friction velocity are determined as 0.72 mm, 0.24 mm, 2.99, and 19.2 m/s, respectively [25].

B. Sharp Fin Model

Fins are made from aluminum (AL-7075). A schematic of the test setup is shown in Fig. 2. Two dowel pins and two bolts are used to position and rigidly mount each fin to the tunnel floor. L_1 represents the length of the fin (i.e., converging section) and L_2 is the length of the constant-area section that is similar to an isolator. Fin-tip-spacing and fin height are labeled as W and H, respectively. DF model is symmetric across the xy-plane. Two different fin angles are designed for the experiments. Figure 2 depicts $\alpha = 10°$ DF configuration. If the fins are swapped, $\alpha = 8°$ DF configuration is obtained. Hence, machining only one pair of fins is sufficient to achieve two different configurations. For 10° DF, $W = 63.50$ mm, $L_1 = 59.83$ mm, $L_2 = 42.80$ mm, and $H = 35.56$ mm. Similarly for 8° DF, $W = 61.44$ mm, $L_1 = 65.65$ mm, $L_2 = 37.11$ mm, and $H = 35.56$ mm.

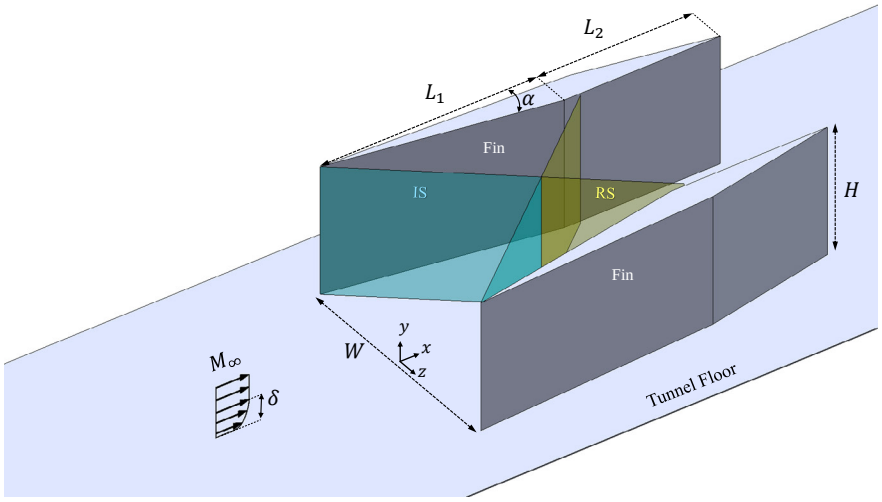

Fig. 2 Perspective view of Double-Fin model. IS: Inviscid Shocks emanating from sharp fin-tips, RS: Reflected Shocks emerging from the shock-crossing, W: Fin-tip-spacing, H: Fin height, α: Fin angle, L: Fin length, M_∞: Freestream Mach number, δ: Incoming boundary-layer thickness.

C. Surface Oil Flow Visualization

Surface oil flow visualization is performed to obtain important features of mean surface flow topology, such as boundary-layer separation and local flow direction. A thin layer of mineral oil mixed together with orange and green fluorescent powder dyes is applied to the surface. A violet LED light (ISSI) with a wavelength of 400 nm is used to illuminate the fluorescent dyes. Images are recorded at 12 Hz using an RGB camera (Prosilica GT) with an exposure time of 400 μs. In order to filter the violet reflections from the background and isolate the fluorescent signal from the dye, an optical long-pass filter is used with a cutoff wavelength of 470 nm.

D. Steady/Unsteady Surface Pressure Measurements

Unsteady pressure measurements are performed using fast-response pressure transducers (Kulite XCQ-062-1BarD, XCQ-062-1.7BarD) to provide an in situ reference for PSP. These pressure transducers are specified with ±0.1% best fit straight line to full-scale output, resulting in a largest uncertainty of ±170 Pa in this study. All pressure transducers are flush-mounted on the tunnel floor and a nitrocellulose adhesive is used to seal and hold them in place. Data are acquired using NI PXIe-1073 chassis with NI PXIe-4331 (24 bits) module. The module is used in full-bridge configuration with a sampling rate of 102.4 kHz. Steady surface pressure data are acquired with a 32-channel pressure scanner (Kulite KMPS-1-32-10psiD) at a sampling rate of 200 Hz where 3424 total samples are acquired for each channel.

E. Pressure-Sensitive Paint (PSP)

In order to obtain the global surface pressure field between the fins, a fast-response Polymer-Ceramic Pressure-Sensitive Paint (PC-PSP) is applied on the tunnel floor with Platinum(II)-5,10,15,20-tetrakis-(2,3,4,5,6-pentafluorphenyl)-porphyrin (PtTFPP) as the photo-reactive luminophore. This technique depends on a chemical process via oxygen

quenching [37]. Considering the overall pressure is linearly dependent on the partial pressure of oxygen, measured pressure becomes a function of oxygen concentration near the luminophore molecules where, PtTFPP is responsive to near 390 nm excitation and it emits near 650 nm [38]. Therefore, a UV light source with a wavelength of 400 nm (ISSI) is used for excitation wherein the camera is fitted with a 610 nm cut-off long-pass filter to remove the reflections of UV excitation. Images are acquired with a 12-bit monochrome high-speed camera (Photron SA-Z) at 20 kHz frame rate (total of 40,000 images). The exposure time is set to 48.39 μs (maximum possible) such that any aliasing effect due to the dynamics of the flowfield is minimized. As shown in Fig. 3, three Kulite pressure transducers are used for the in situ calibration of unsteady PC-PSP. Upstream-facing half-circles are used as the PSP "patch" areas to avoid contamination from pressure transducers. Although the pressure transducers are carefully located to be flush with the surrounding paint, potential local flow perturbations are still possible in case the transducers are not perfectly flush. Each PSP patch consists of approximately 115 pixels to spatially average the intensity values for the in situ calibration. By using the method of least-squares, a linear curve fit is applied as indicated in the reduced Stern-Volmer equation [37]:

$$\frac{P}{P_{\text{ref}}} = A(T) + B(T)\frac{I_{\text{ref}}}{I} \tag{1}$$

where, $A(T)$ and $B(T)$ are the temperature-dependent empirical in situ coefficients, I is the spatially averaged intensity values corresponding to the related PSP patch during the run, I_{ref} is the spatially averaged intensity values in the related PSP patch region under the atmospheric condition when the tunnel is off, P is the desired pressure (Kulite pressure transducer signal) in physical units, and P_{ref} is the absolute pressure under atmospheric condition. The frequency response of the PSP paint is analyzed by the coherence function between the unsteady Kulite pressure transducer signal and the signal acquired from the corresponding spatially averaged PSP patch area as illustrated in Fig. 3. The magnitude-squared coherence function is defined as [39]:

$$\left|\gamma_{xy}(f)\right|^2 = \frac{\left|G_{xy}(f)\right|^2}{G_{xx}(f)\,G_{yy}(f)} \tag{2}$$

where, $G_{xy}(f)$ is the cross-spectral density as a function of frequency, $G_{xx}(f)$ and $G_{yy}(f)$ are the autospectral density functions for the unsteady PSP and surface pressure signals, respectively. When the signals are highly correlated at a specific frequency, the coherence function approaches to unity. As seen from Fig. 3, PSP paint is responsive roughly up to 8 kHz with a coherence value above 0.5 which is in good agreement with previous studies [16, 37, 40]. Therefore, 8 kHz ($St_\delta = 0.055$) frequency response is determined as a reasonable cutoff for the unsteady PSP measurements in the present study. The largest 2σ uncertainty within the PSP patch measurements is estimated as ± 1.5 kPa.

Additionally, to acquire steady pressure fields, a Binary Fluoride-Isopropyl-Butyl Pressure-Sensitive Paint (BI-FIB PSP) is used [41]. An RGB camera (Prosilica GT) recorded the emission signals from two different luminophores

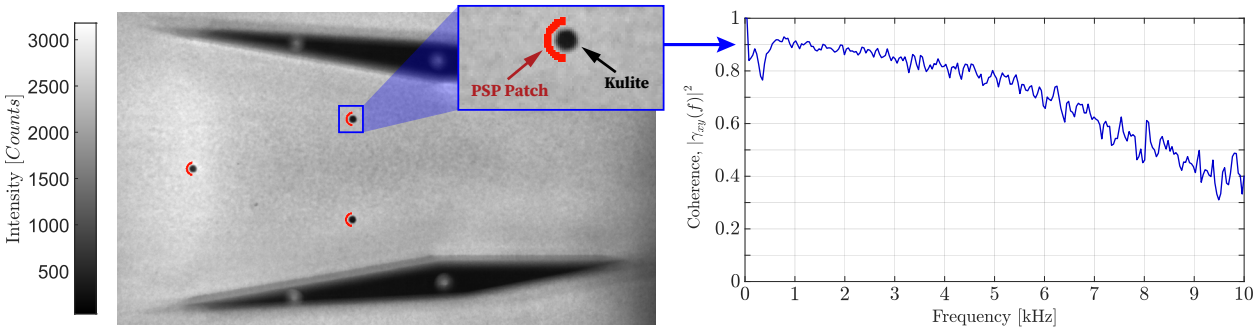

Fig. 3 An instantaneous unsteady PSP image with three Kulite unsteady pressure transducers (black circles) and upstream-facing half-circle PSP "patches" (colored red) are shown for the in situ calibration (on the left). The frequency response coherence of the Kulite and the spatially averaged PSP patch area for the zoomed region is shown on the right.

where the red channel of the RGB sensor captures the pressure- and temperature-sensitive signal and the green channel acquires the only temperature-sensitive signal. A long-pass filter with a 470 nm cut-off is used to remove the 400 nm excitation wavelength. Images are acquired at a frame rate of 16 Hz (total of 1000 images) with 2500 μs exposure. The ratio-of-ratios of the red and green channels corrects the local temperature effects in the pressure signal [41, 42]:

$$\frac{I_{\text{ref}}}{I} = \frac{I_{R_{\text{ref}}}/I_{G_{\text{ref}}}}{I_R/I_G} \tag{3}$$

where, I_{ref} is the intensity field under the atmospheric condition when the tunnel is off, I is the intensity field during the run, and R and G subscripts denote the red and green channels of the RGB sensor, respectively. In the present study, the largest 2σ uncertainty within the PSP patch measurements is estimated as ±0.5 kPa for the steady PSP technique. Supplementary elucidations on the use of PSP techniques to study different flow regimes in various wind tunnel applications are available in Refs. [16, 41, 43–45].

III. Results and Discussion

A. Comparison between Single-Fin and Double-Fin SBLI

1. Mean Flowfield Surface Features

In order to examine the surface flowfield features of DF SBLI as well as to compare the surface properties to SF SBLI, oil flow visualization is performed as shown in Fig. 4. Both the SF and DF have a 10° fin angle with respect to the incoming freestream of Mach 2. In the SF case (see Supplementary Video S1 for the corresponding time lapse), it is observed that the oil streaks are deflected near the fin-tip, and the oil upstream of the fin coalesces along an oblique line (the dark region under the dashed magenta line in Fig. 4a). Referred to as the Primary Separation (PS), it is where the flow separates from the surface and lifts-off away from the tunnel floor. Taking a closer look at the region upstream of

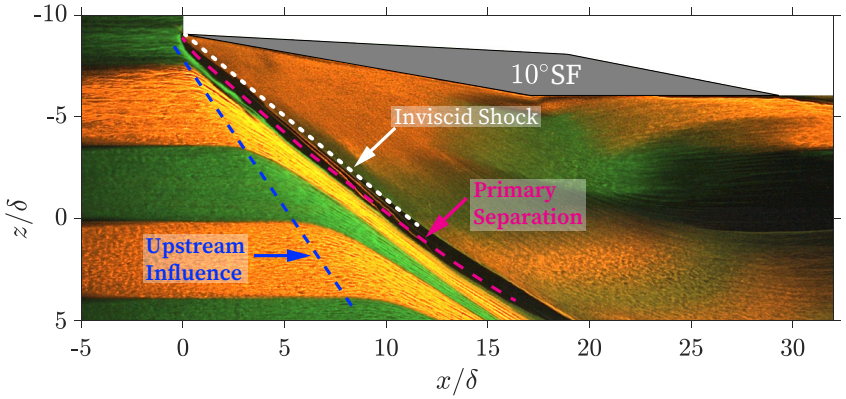

(a) 10° Single-Fin

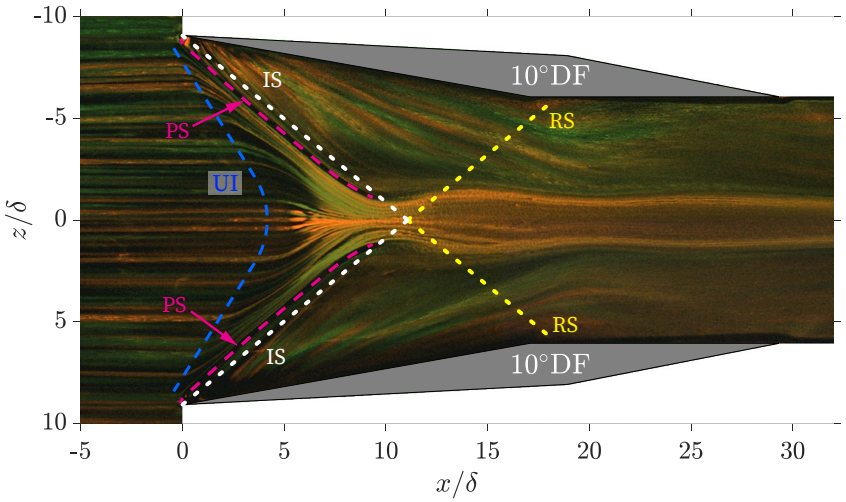

(b) 10° Double-Fin

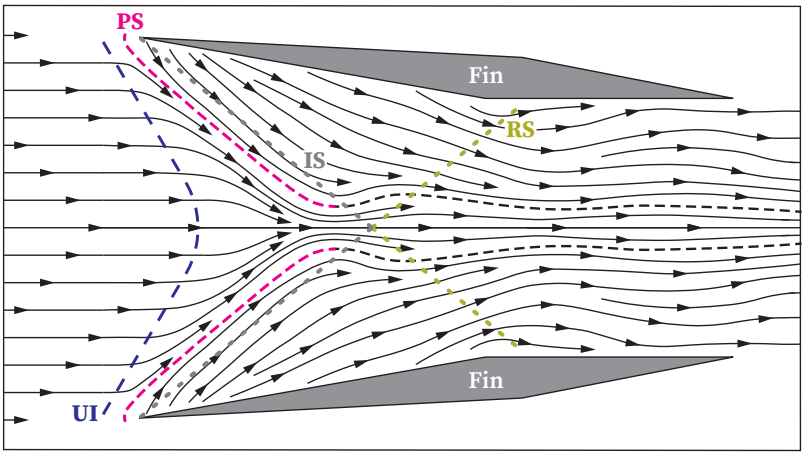

(c) Sketch of Double-Fin interaction showing key surface features.

Fig. 4 Surface oil flow visualization showing oil streak lines. Comparison of surface flow topology reveals the similarities and differences between 10°SF and 10°DF. Corresponding time lapses are shown in Supplementary Videos S1 and S2. Flow direction is from left to right. UI: Upstream Influence, PS: Primary Separation, IS: Inviscid Shock, RS: Reflected Shock.

PS, it is seen that the oil streaks oriented parallel to the incoming flow start to deflect away from the fin (blue dashed line in Fig. 4a), referred to as the Upstream Influence (UI) line. The region between UI and PS is the "intermittent separation" where the two lines roughly mark the upstream and downstream extent of the front-foot of λ-shock (see Fig. 1). This front shock is also referred to as the separation shock.

Figure 4b shows the oil flow visualization of DF SBLI (Supplementary Video S2). A subsidiary schematic of the oil flow visualization is illustrated in Fig. 4c to emphasize the oil streak paths. Similar to the SF case, the oil streaks deflect in the same manner near the fin-tips at both the upper and lower fins. Since the fin angles at the top and bottom are the same (10°), the flowfield is symmetric across the centerline ($z/\delta = 0$). Hence, one may also think of this as a SF SBLI where the interaction reflects from an imaginary inviscid wall situated along the centerline. However, this analogy breaks down when the flow approaches the region near the centerline as seen in Fig. 4b. Here, the PS lines originated from both fins approach each other towards the centerline but do not intersect. Instead, they curve parallel to the centerline. On the other hand, UI lines of SF and DF cases are almost identical (up to about 2δ away from the centerline). This suggests the quasi-conical symmetry also applies to DF up to a limited extent and subsequently breaks down near the centerline. DF flow features near the central region are discussed in detail in Sec. III.B.1 by comparing two flowfields with different fin angles.

2. Mean Surface Pressure Field

The global mean surface pressure field is obtained by using steady and unsteady PSP methods for the same cases of which oil flow visualization is shown in Fig. 4. Steady PSP (BI-FIB PSP) is performed not only to capture the mean surface pressure features, but also to validate unsteady PSP results since fast-response single-luminophore PC-PSP has no correction capability for localized illumination and temperature variations. The mean PSP results for the SF and DF configurations are shown in Fig. 5, where the left and right images show the SF and DF SBLI, respectively. The top half of each image depicts the time-averaged unsteady PSP results, whereas the bottom half illustrates the averaged steady PSP results (flipped vertically for direct comparison). Even though only half of the images are used for comparison purposes, it is important to note that the full flowfield exhibits a high degree of symmetry for the DF interactions, as the DF geometry itself is symmetric. For both the SF and DF SBLI, pressure iso-contours of unsteady PSP agree well with the contours of steady PSP as shown in Fig. 5. The most salient difference, which is still not very substantial, is marked with the blue-dashed box in Fig. 5b. This region corresponds to the area beneath the separation vortex. Pressure values in this local region are lower in the unsteady PSP results compared to steady PSP. In the present study, steady PSP is considered as a more accurate method compared to unsteady PSP since steady PSP is capable of temperature correction. Whereas the unsteady PSP response is a function of both pressure and temperature, and lower temperature would introduce lower pressure gain for the unsteady PSP. Thereby, it is expected that this locally lower temperature region is caused by the increased convection under the separation vortex which quickly cools the PSP paint during the

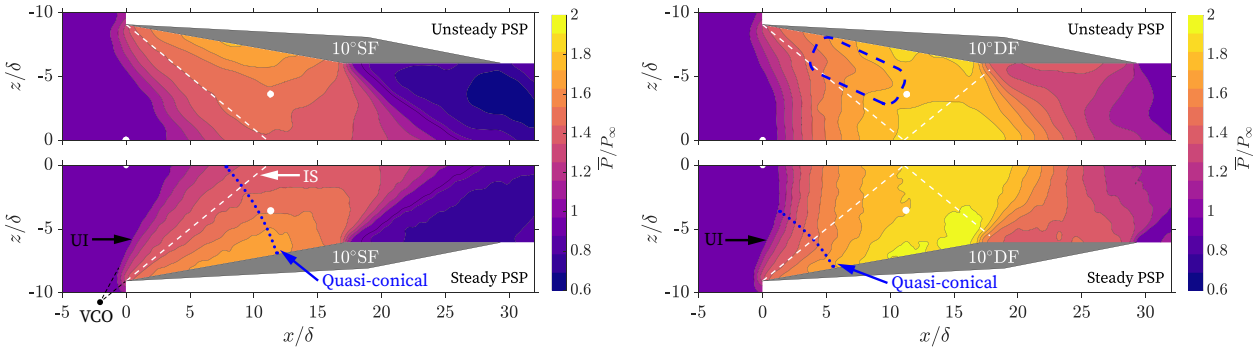

(a) 10° Single-Fin **(b) 10° Double-Fin**

Fig. 5 Composite image showing the comparison between the surface pressure fields of time-averaged unsteady PSP (Top) and steady PSP (Bottom). White circles show the location of Kulite unsteady pressure transducers. Surface features UI and IS are indicated as in Fig. 4. Blue-dashed box highlights a region of significant difference between unsteady and steady PSP. The extent of the quasi-conical region is marked with blue-dots. Flow direction is from left to right.

run. Additionally, the 8°DF, to be discussed later in Sec. III.B.2, shows similar localized temperature effect, and the 8°SF has similar iso-contours as the 10°SF, but it is not provided here for brevity. Despite these differences observed due to temperature sensitivity, the overall agreement between steady PSP and unsteady PSP is considerably good and one can use either formulation of PSP to extract the mean pressure flowfield.

The pressure field for 10°SF is examined in Fig. 5a. Overall, the pressure begins to increase at the UI line (front-foot of the λ-shock), and a rise is seen as one goes across the separation with the maximum pressure in the vicinity of the fin, suggesting the primary attachment to be on the surface of the fin near the fin-plate junction. Based on prior studies [12, 16, 18], the high pressure occurs at/near the primary attachment line, and this is consistent with the observations of the present study. Further downstream, near the corner where the fin surface turns parallel to the incoming flow direction, the pressure begins to relax back to freestream values (purple contours). This is expected due the expansion fan that originates at this junction. Away from the fin, the iso-contours are almost straight lines, which is the signature of the quasi-conical region. Closer to the fin-tip, pressure iso-contours start to curve towards the fin-tip wherein this region is referred to as the inception zone.

When comparing the SF to the DF flow, the pressure fields near the fin-tips are very similar, i.e., the signature of inception zone and quasi-conical nature of the flowfield is unchanged. However, quasi-conical symmetry progressively breaks down for the DF as one approaches the centerline where the pressure iso-contours start to turn perpendicular to centerline as seen in Fig. 5b.

The PSP results for DF show that UI is pushed further upstream near the centerline since pressure starts to rise earlier when compared to SF. Starting from the UI line along the centerline, the gaps between the iso-contour levels increase downstream. This means surface pressure first increases rapidly starting from the UI, then it continues to increase more gradually. Peak pressure occurs after the shock-crossing on the centerline and starts to decrease as it

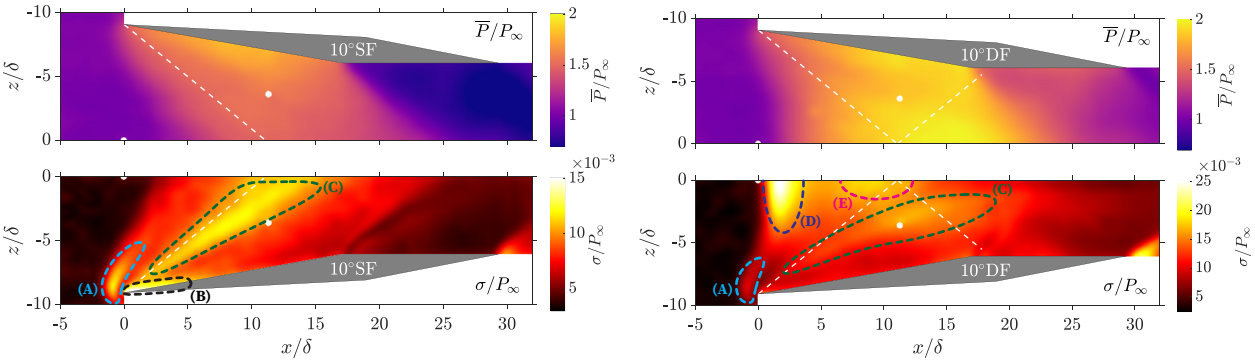

(a) 10° Single-Fin **(b) 10° Double-Fin**

Fig. 6 Composite image showing the comparison of surface pressure field from time-averaged unsteady PSP (Top) and standard deviation normalized with freestream pressure (Bottom). Features A-E are discussed in the text.

passes throught the expansion fans farther downstream. As a result, DF has a greater pressure increase compared to SF, which is expected due to the additional shock compression. Additionally, it should be noted that the UI location is observed further upstream compared to the surface oil flow results discussed earlier. This result can be attributed to the surface roughness of the PSP paint which is significantly greater when compared with the surface oil flow application. This is also a reminder that whereas surface flow visualization techniques are powerful, they are intrusive to the flowfield and may alter the boundary-layer characteristics developed over a smooth flat plate.

3. Unsteady Surface Pressure Field

In order to examine the unsteady characteristics of the pressure field, the time-averaged unsteady PSP (top half) and the corresponding standard deviation of the surface pressure fluctuations normalized with freestream pressure (bottom half, images are flipped vertically) are illustrated in Fig. 6. For the SF case (Fig. 6a), high pressure fluctuations are observed at three locations: just upstream of the fin-tip/plate junction (region *A*), right at the junction of the fin surface and the plate (region *B*), and under the separation vortex (region *C*). The main reason for high unsteadiness upstream of the fin-tip (region *A*) is likely a local bow-like shock situated in front of the sharp-fin close to the plate inside the boundary layer. Even though sharp-fins generate attached oblique shocks in the inviscid region, since the local Mach number decreases towards the tunnel floor inside the boundary layer, at some point the fin angle exceeds the maximum oblique shock angle that the local Mach number can support, and the shock detaches inside the boundary layer. This detached shock structure just upstream of the fin-tip is attributed to an open separation bubble [25, 46]. Furthermore, the extension of this unsteadiness (region *A*) weakens along with the UI away from the fin-tip. Under the separation vortex (region *C*) in the quasi-conical region, the width of the unsteadiness field spreads out away from the fin-tip. This is expected since the separation vortex grows conically. Comparing these SF unsteadiness features with the DF case as depicted in Fig. 6b, a similar phenomenon is observed in the upstream part of the interaction (region *A*), but it merges with a relatively large elliptic-like region near the centerline (region *D*) whose intensity dominates the rest

of the field. The region *C* in Fig. 6a under the separation vortex near the fin-tip is not as obvious for the DF case in Fig. 6b since the color-scale range is increased due to higher unsteadiness levels in the DF flowfield. However, it is still discernible in Fig. 6b where it spreads out and curves parallel to the centerline, and its magnitude further increases before it interacts with the expansion fan. Also, the curve pattern in region *C* is consistent with the curve pattern of the PS line from the oil flow visualization in Fig. 4b. Additionally, it should be noted that the unsteadiness just upstream of the shock-crossing (region *E*) is another region which shows relatively high unsteady pressure values and distinguishes the DF interaction from SF SBLI.

To understand and explore the properties of unsteady surface features, correlation coefficients are computed to obtain a visual map of the interaction. In these analyses, Pearson correlation coefficient (normalized covariance) is used

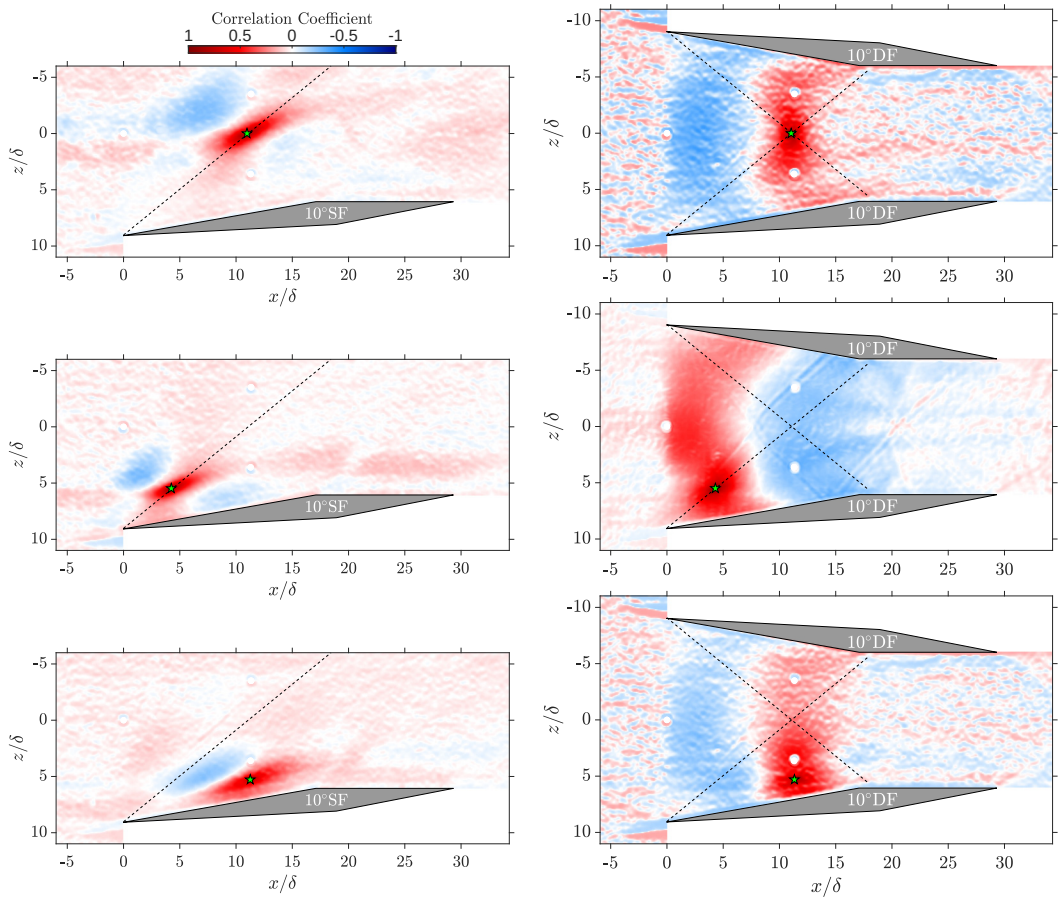

(a) 10° Single-Fin **(b) 10° Double-Fin**

Fig. 7 Comparison of correlation coefficients of unsteady pressure fluctuations between 10°SF and 10°DF. Obtained from unsteady PSP. The star symbol in green shows the reference point where the rest of the pressure fluctuation field is correlated with. Black dashed lines indicate inviscid oblique shocks.

which is a measure of linear dependence of two random variables [39]:

$$\rho_{xy} = \frac{\mathrm{cov}\,(\vec{x},\vec{y})}{\sigma_x \sigma_y} = \frac{1}{N-1}\sum_{k=1}^{N}\left(\frac{x_k-\mu_x}{\sigma_x}\right)\left(\frac{y_k-\mu_y}{\sigma_y}\right) \tag{4}$$

where, ρ is the correlation coefficient, $\vec{x}$ and $\vec{y}$ are the time series vectors of mean-subtracted unsteady PSP signal (pressure fluctuations) at two different locations, N is the length of the time signal, μ is the mean, and σ is the standard deviation. Figure 7 compares the correlation coefficient field of 10°SF (left column) to 10°DF (right column) at several different key reference points. Dashed line indicates inviscid oblique shock direction. The star symbol in green indicates the reference point to which the rest of the unsteady pressure field is correlated. Red scale indicates the level of correlation in the same phase wherein blue scale indicates the correlation in the opposite phase. On SF cases (Fig. 7a), it is observed that the highly correlated regions are localized and aligned with the inviscid oblique shock wave (black dashed line) direction. On the other hand, DF cases (Fig. 7b) show that the highly correlated regions span all the way up to the top and bottom fins in the interaction region and looking almost vertically aligned (perpendicular to the freestream direction). Having red and blue regions back to back suggests the existence of traveling waves of pressure fluctuations, but it is not possible to determine the direction with this analysis. However, the direction of these waves is clarified through SPOD analysis that are presented later in this section. Furthermore, it is worthy to note that no correlation with the freestream is observed on any of these analyses, thereby the wave patterns are generated by the fins.

It is important to understand the spectral content of the unsteady flow. For this purpose, Power Spectral Density (PSD) of the pressure fluctuation field is calculated by using Welch's method of periodograms [47]. The green-dashed lines in Fig. 8 show the location where the spectrogram is obtained and shifted slightly from the centerline to avoid the

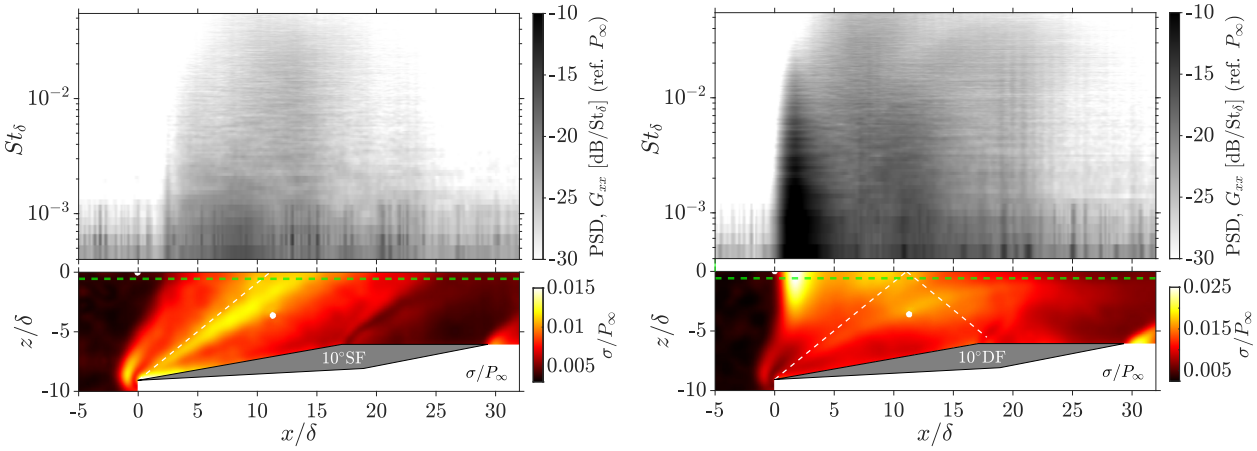

(a) 10° Single-Fin **(b) 10° Double-Fin**

Fig. 8 Comparison of near-centerline Power Spectral Density (PSD) between 10°SF and 10°DF. Obtained from unsteady PSP. Green-dashed lines plotted on the standard deviation field (bottom) show the location where the PSD field (top) is extracted from. White dashed lines indicate inviscid oblique shocks.

unsteady pressure transducer. Figure 8a shows a composite image of the PSD of 10°SF on the top and the standard deviation field is presented as an overview at the bottom. Overall, the pressure spectrogram does not contain any distinct tones which is typical of broad-band, turbulent flows. The intensity of the spectra, in general, monotonically decreases with increasing St_δ. Beneath the freestream ($x/\delta < 2.5$) on the surface of the tunnel floor, where the flow remains unaffected by the interaction, high frequency fluctuations are insignificant. Near the UI ($x/\delta \approx 2.5$), high frequencies rapidly gain energy and further downstream the spectral values gradually decrease towards the levels observed underneath the unperturbed flow. By contrast, Fig. 8b shows the pressure spectrogram for 10°DF. Overall, the spectral behavior of DF and SF reveals increased intensity at higher frequencies downstream of the UI that proceeds to decrease while passing through expansion fans. However, since the DF SBLI is a stronger interaction, higher intensities in the spectral content distinguish it from SF SBLI. In addition, higher unsteadiness values at lower frequencies just downstream of the UI ($1 < x/\delta < 3$) are prominent at the locations of high standard deviation as seen in Fig. 8b.

Having time-resolved full-field measurements enables the extraction of unsteady (spatially coherent) flow features related to each frequency through the Spectral Proper Orthogonal Decomposition (SPOD) algorithm, which will enable further insight into the flow physics related to this flow field. SPOD [48] is a strong analytical tool to decompose spatial mode structures at different frequencies. A streaming SPOD algorithm [49] is employed in this work to highlight the relevant flow physics present in this data set. The SPOD is a variant of POD that utilizes the Welch's periodogram averaging method [47] to extract modal behavior coherent in both space and time, and can be seen as a sophisticated, full-field Fourier analysis tool. The mode shapes are complex-valued and single-frequency, thus phase relationships between different spatial locations can be unveiled and visualized. In the SPOD analyses presented in this paper, a total of 40,000 snapshots acquired at 20 kHz are used for each case. A Hamming window size of 512 is applied with a 75% overlap resulting in a total of 309 blocks. The streaming SPOD algorithm is utilized to calculate a total of 50 modes with a frequency resolution of $\Delta St_\delta = 2.681 \times 10^{-4}$. The spatial region of interest for the SPOD analyses is the surface between the Double-Fins, which is fully depicted in the appropriate figures.

Figures 9 and 10 illustrate the normalized eigenvalue spectra of the first five SPOD modes out of a total of 50 modes, along with the mode shapes of the real part of the first mode at selected frequencies for 10°SF and 10°DF cases, respectively. Typically, the first few modes are sufficient to capture the pressure patterns which are representative of coherent flow structures as they contain most of the energy in the flowfield. Noting that the y-axis of the spectra is logarithmic, the energy of the second mode is substantially smaller than the first mode (Fig. 10), a trend that continues with increasing mode numbers. Therefore, only the first mode shapes are shown for brevity. Both the SF and DF spectra are broad-band and monotonically decreasing with increasing St_δ, and no peaks of interest or humps exist, which is expected, recalling the unsteady analysis previously discussed in this section. Therefore, the mode shapes depicted in the corresponding figures are thoughtfully selected to capture the overall flowfield characteristics, ensuring a well-distributed sampling across the frequencies of interest. Multiplying the mode by $e^{i\theta}$ advances the mode in time, where $\theta = 2\pi f t$ is

the phase angle of the corresponding frequency f. When the modes are animated this way, it is observed the mode shapes at all frequencies propagate downstream which indicates downstream-traveling coherent pressure waves on the surface. The Supplementary Videos S3 and S4 provide further evidence of these downstream-traveling wave-like structures.

Overall, the mode shapes for 10°SF illustrate that the coherent wave structures (alternating red-blue regions in Fig. 9) are inclined in the direction of UI. At low-frequencies (Fig. 9a-b), these waves are generated along the UI and they travel downstream spanning the entire SBLI region. The mode shape at $St_\delta \approx 0.002$ (Fig. 9a) clearly captures the local bow-like shock region inside the boundary layer in front of the sharp fin-tip as shown in region *A* in Fig. 6a. This suggests that the bow-like shock experiences low-frequency oscillations. The mode shape in Fig. 9c corresponds to the small peak at $St_\delta \approx 0.006$ in the spectra. This specific mode shape shows sharp features parallel to the fin-walls near the fin-boundaries and upstream of the fin-tip, indicating vertically oriented fluctuations in the surface

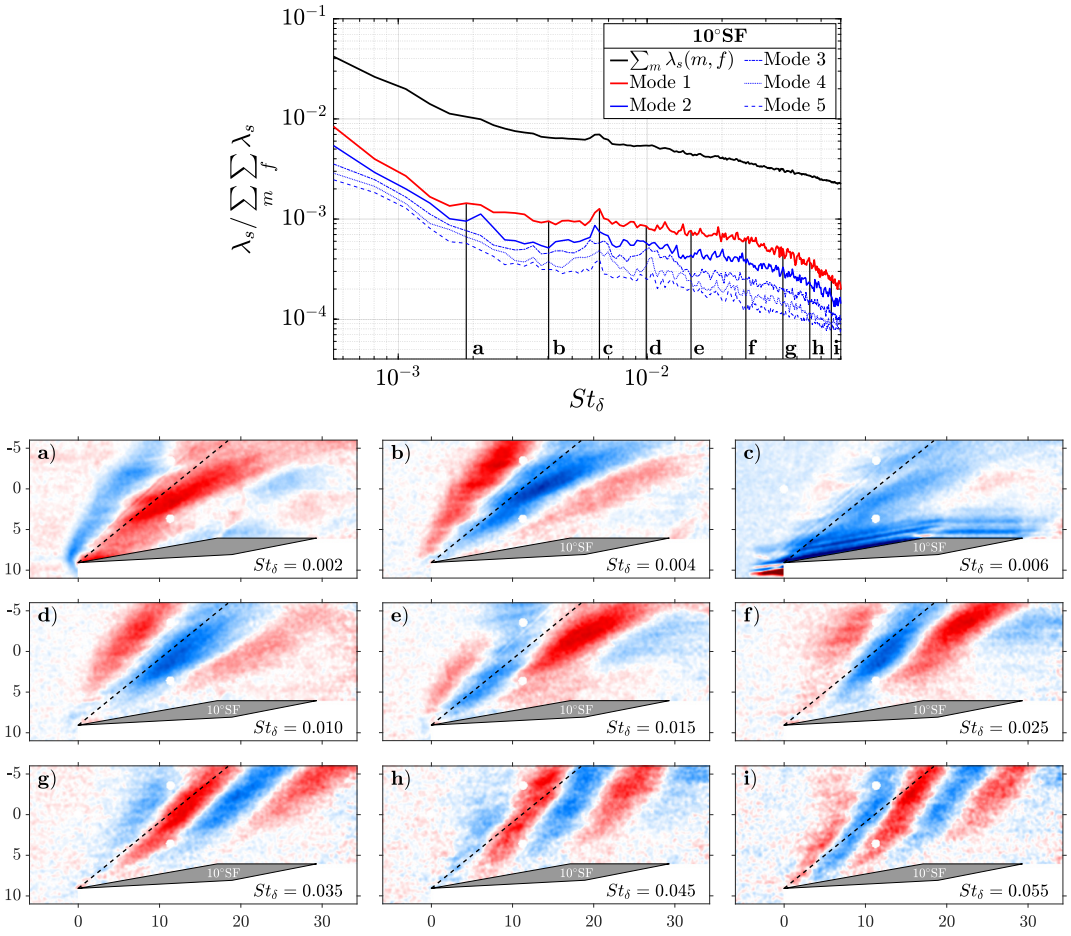

Fig. 9 Normalized eigenvalue spectra and the real part of the first mode of SPOD extracted from unsteady PSP at various frequencies for 10° Single-Fin. Red and blue color scales are symmetric and arbitrary, and white color represents zero. Mode shapes are animated in the Supplementary Video S3. Black dashed lines indicate inviscid oblique shocks.

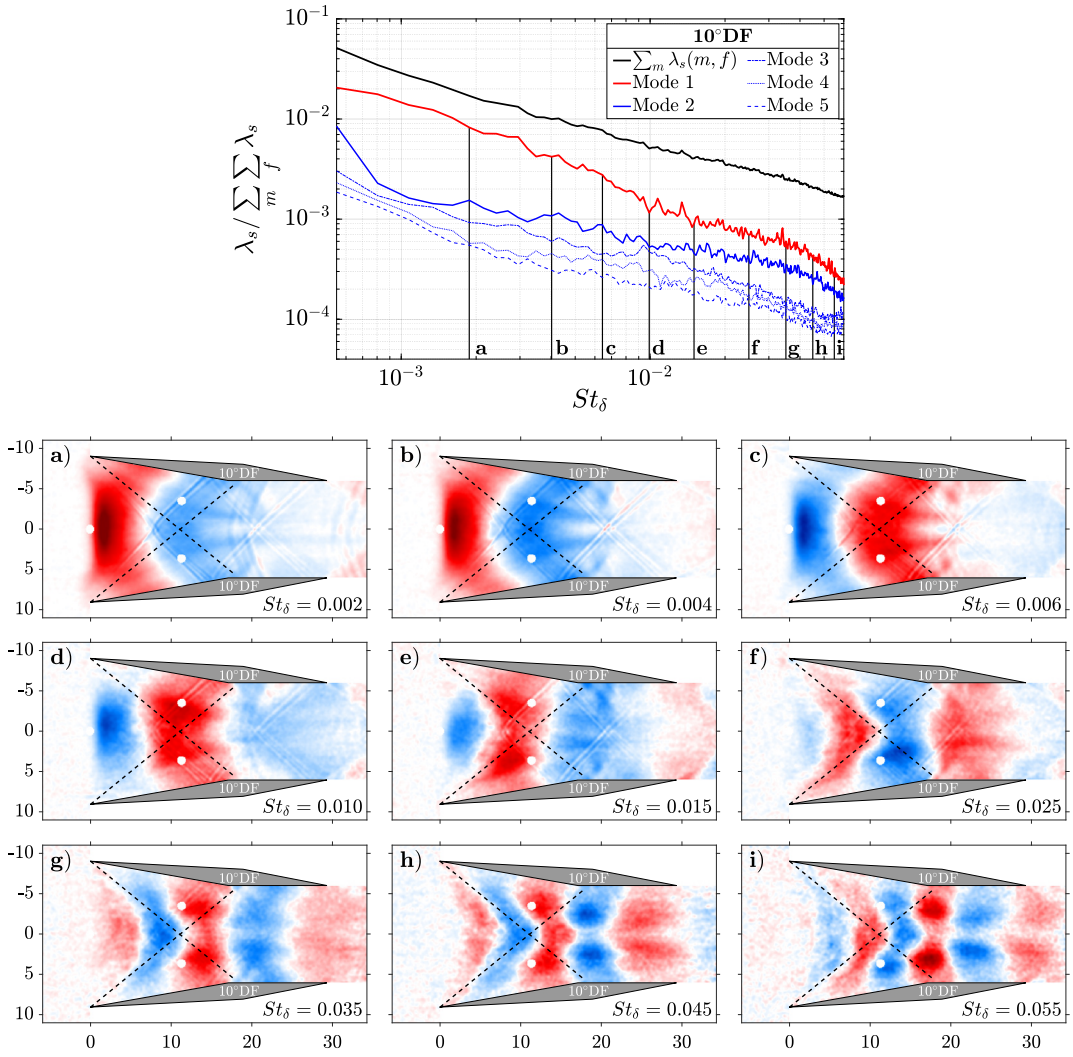

Fig. 10 Normalized eigenvalue spectra and the real part of the first mode of SPOD extracted from unsteady PSP at various frequencies for 10° Double-Fin. Red and blue color scales are symmetric and arbitrary, and white color represents zero. Mode shapes are animated in the Supplementary Video S4. Black dashed lines indicate inviscid oblique shocks.

pressure. Supplementary Video S3 demonstrates that these features are also blended with flowfield-induced oscillations. Considering the governing behavior of the mode shapes at various frequencies and modes, it can be reasonably inferred that this specific mode shape does not fully represent the underlying flow physics. This observation leads us to speculate that the vertically oriented fluctuations, occurring at relatively low frequency, could be attributed to vibrations present during the wind tunnel runs or vibrations transmitted to the camera attached to the tunnel's structural frame, despite the images having been registered prior to SPOD processing. Recalling the Pearson correlation coefficient analysis presented earlier in this section, similar features mostly just upstream of the fin-tips are also observed in those analyses (see Fig. 7). Since the correlation coefficient technique suffers from the lack of frequency decomposition, this vibration related mode at a specific frequency blends with the modes related to the flowfield dynamics at other frequencies, which precludes to

filter the only flowfield related structures. As a result, the bow-like shock region is therefore suppressed by this vibration related mode and the correlation coefficient analysis fails to capture the bow-like shock region whereas SPOD analysis successfully filters the vibration related mode from the modes related to flowfield dynamics. For $St_\delta > 0.01$ (Fig. 9d-i), the mode shapes show a decrease in the wavelength of the downstream-traveling surface pressure waves as the temporal frequency increases.

When the SPOD results of 10°DF are examined, the low-frequency unsteadiness ($St_\delta < 0.01$) is evident in the pressure spectra which is consistent with the results obtained from near-centerline PSD analysis (see Fig. 8b) presented earlier. The first mode shapes contributing to the low-frequency unsteadiness are shown in Fig. 10a-d, where the pressure waves are produced at the vicinity of the centerline starting near the UI. This region corresponds to region *D* in Fig. 6b, where high levels of unsteadiness is present. In general, these waves span the entire SBLI field between the fins perpendicular to the freestream direction unlike the results obtained from SF. At higher frequencies ($St_\delta > 0.01$), as shown in Fig. 10e-i, wave structures start to curve somewhat similar to SF mirrored along the centerline since it is a symmetric interaction, and the wavelength of the downstream-traveling surface pressure waves decreases with increasing St_δ. Furthermore, the bow-like shock region is not clearly visible in these first mode shapes in the given color scale range since the unsteady dynamics near the centerline dominate the overall strength on the rest of the DF flowfield. It is worth noting that the symmetric nature of the DF geometry inherently leads to a high degree of flowfield symmetry, which is clearly observed in the first mode shapes. However, this symmetric mode shape structure in higher modes does not always occur. For instance, second mode of 10°DF (see Supplementary Video S5) exhibit downstream-traveling anti-symmetric mode shapes.

B. Effect of Interaction Strength (Fin Angle)

1. Mean Flowfield Surface Features

To examine the effect of fin angle, oil surface flow visualization is performed for 8° and 10°DF, and the results are compared in Fig. 11. This is a composite figure wherein one half of the 8°DF (top) is compared to one half of the 10°DF flowfield (bottom). Corresponding full-field time lapses are also available in Supplementary Videos S6 and S2, respectively. Although the entire surface oil visualization fields are not presented, both of the DF interactions have similar symmetric features where the symmetry plane is along the centerline. The primary separation lines for both cases are emphasized with the purple-dotted lines. As seen in Fig. 11, the PS line is reasonably straight in the quasi-conical region and it begins to curve towards the freestream direction as one moves away from the fin and approaches the interaction line of symmetry or centerline. This change in direction roughly corresponds to the end of the quasi-conical region where the interactions formed from upper and lower fins are now influenced by both. Outside the quasi-conical region, the two PS lines first turn parallel to the centerline, then they diverge slightly before they converge again. This feature creates a converging-diverging-converging (CDC) shape along the interaction centerline. Since the upper and the

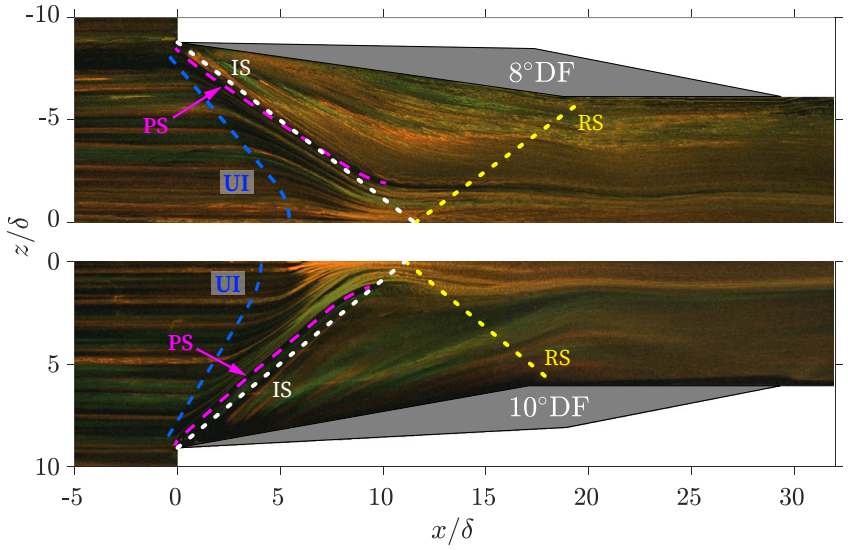

Fig. 11 Surface oil flow visualization showing the surface streak lines of 8° (top) and 10° (bottom) Double-Fin. Corresponding time lapses are available in Supplementary Videos S6 and S2, respectively. Flow direction is from left to right. UI: Upstream Influence, PS: Primary Separation, IS: Inviscid Shock, RS: Reflected Shock.

lower PS lines do not cross and no other separation line is observed in the centerline, no flow separation occurs in this CDC region for either of the cases. It is worth noting that only primary separation is observed on 8°DF and 10°DF cases with no evidence of centerline separation nor secondary separation; hence, both of these interactions may be classified as "weak" interactions according to the flow separation features [21]. The oil streaks on the surface show that all the freestream flow upstream of the fins in the inner layer of the incoming boundary layer funnel through the "throat" of this CDC region. Since the strength of the oblique shocks produced by 8°DF is lower than 10°DF, the separation vortex is weaker on 8°DF. This addresses that the PS line on 10°DF can penetrate further towards the interaction centerline before they bend parallel to it. As a consequence, the throat width at the converging-diverging section of the CDC region of 10°DF is smaller when compared with 8°DF. In addition, it is observed that the PS line sits just upstream of the inviscid shock on 10°DF wherein the PS line on 8°DF crosses the inviscid shock, suggesting that PS is pushed further upstream as the interaction strength increases.

2. Mean Surface Pressure Field

Figure 12 illustrates the comparison of the mean surface pressure fields of 8° and 10°DF at Mach 2. Overall, higher interaction strength for the 10°DF case results in higher overall surface pressure in between the fins. As mentioned earlier, pressure iso-contours start to turn perpendicular to the centerline away from the quasi-conical region. This behavior is the signature of the DF interaction and is seen on both of the cases as depicted in Fig. 12. By using the origin as the base, the UI location near centerline for the 10°DF is upstream by more than 2δ compared to the location on the 8°DF. However, if the origin is changed to the shock-crossing (intersection of the two white dashed lines), the

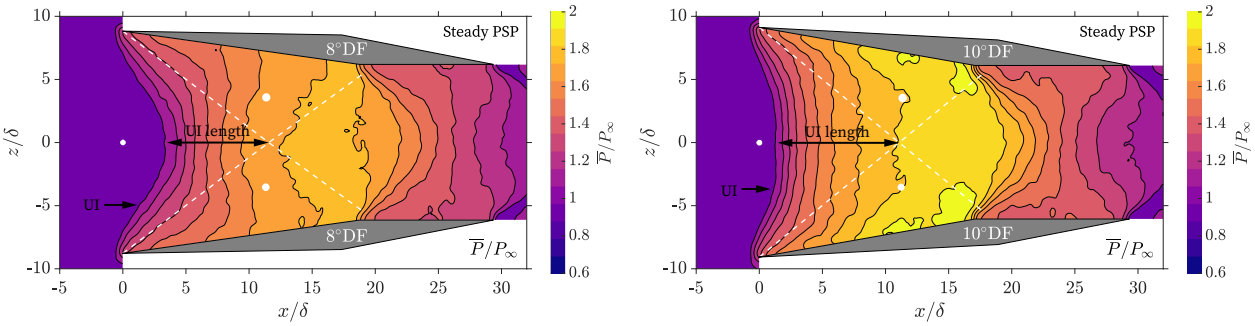

(a) 8° Double-Fin **(b) 10° Double-Fin**

Fig. 12 Comparison of mean surface pressure field between 8° and 10°DF. Obtained from steady PSP. Flow direction is from left to right. White dashed lines indicate inviscid oblique shocks.

difference between the UI lengths in these two cases is less significant; that is 1.6δ; UI length is defined as a measure of distance between UI location and shock-crossing which is emphasized by the black arrows in Fig. 12 for clarity. Based on the premise that the fin-tip-spacing is almost identical for these two cases, the difference between UI lengths is a result of different interaction strengths. To be more explicit, interaction strength can be defined in a quantitative manner by introducing the normal Mach number M_n. Normal Mach number ($M_n = M_\infty \sin\beta$) is the component normal to the inviscid oblique-shock generated by the sharp fin wherein the shock angle β is defined by freestream Mach number M_∞ and fin angle α through oblique-shock relations. Hence, M_n increases with both increasing freestream Mach number, and fin angle. In stronger interactions (i.e., larger M_n), the size of the λ-shock increases where the front-foot of the separation shock is further upstream from the inviscid shock location. Hence, when two λ-shocks cross each other, the size of the interaction (i.e., the upstream extent underneath the SBLI region) grows relative to the strengths of the crossing shocks. Therefore, by definition, UI length is expected to grow for higher fin deflection, as is the case when comparing 8°DF to 10°DF. It should be noted that the normal Mach number is not the only variable deciding UI length.

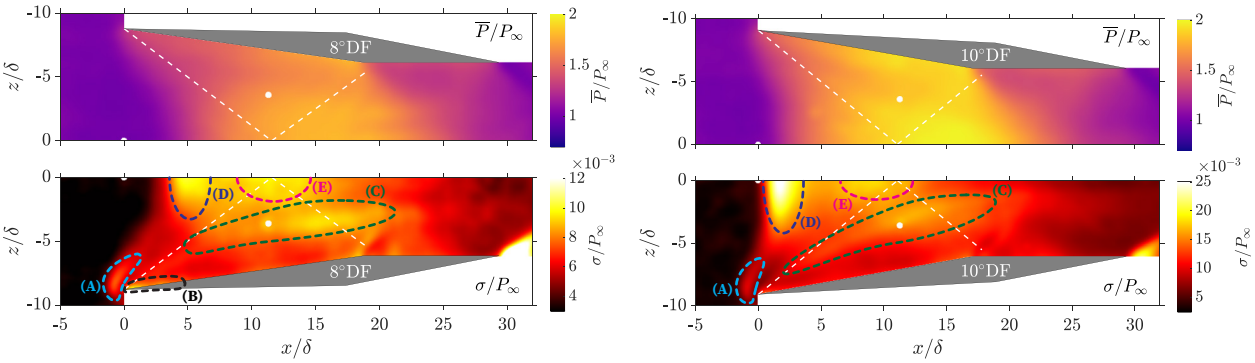

(a) 8° Double-Fin **(b) 10° Double-Fin**

Fig. 13 Composite image showing the comparison of surface pressure field from time-averaged unsteady PSP (Top) and standard deviation normalized with freestream pressure (Bottom). Features A-E are discussed in the text.

Due to quasi-conical symmetry, UI length is also a function of fin-tip-spacing and the details are elaborated in Sec. III.D.

3. *Unsteady Surface Pressure Field*

In order to compare the effect of fin angle on unsteady characteristics of the pressure field, the time-averaged unsteady PSP (top) and the corresponding standard deviation of surface pressure fluctuations normalized with freestream pressure (bottom, images are flipped vertically) are illustrated in Fig. 13 for the 8° and 10°DF cases. In general, the unsteady fields of the two cases are similar where some of the regions of interest were previously discussed in Sec. III.A.3 for 10°DF. The most notable difference is the location of the elliptic-like region at the UI in the centerline (region *D*), which is located further upstream for the stronger interaction (10°DF). This high unsteadiness region is almost twice as prominent in the amplitude when 10°DF is compared with 8°DF. For 8°DF (Fig. 13a), the unsteady pressures in region *D* are comparable to the region of the inviscid shock-crossing (region *E*). By contrast, as the interaction strength

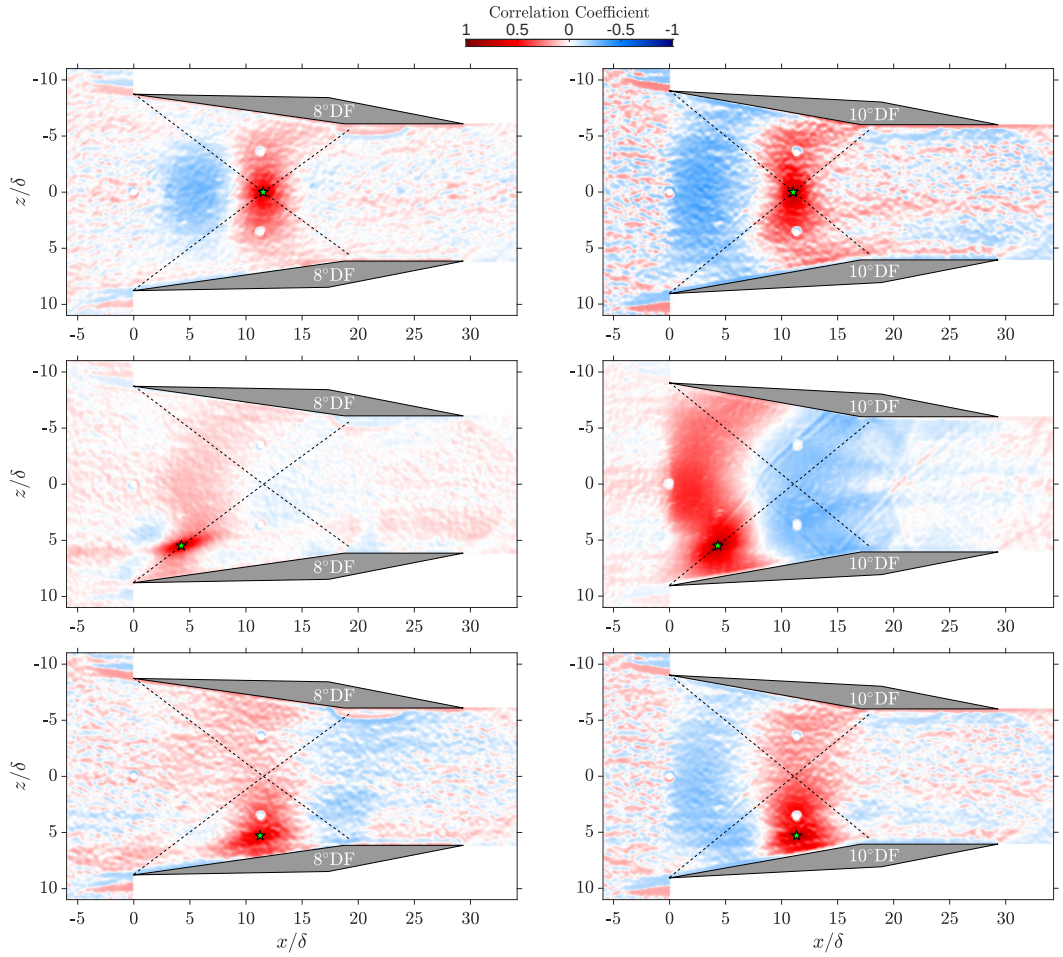

(a) 8° Double-Fin **(b) 10° Double-Fin**

Fig. 14 Comparison of correlation coefficients of unsteady pressure fluctuations between 8°DF and 10°DF. Obtained from unsteady PSP. The star symbol in green shows the reference point where the rest of the pressure fluctuation field is correlated with. Black dashed lines indicate inviscid oblique shocks.

is increased as seen in the 10°DF case (Fig. 13b), the unsteady pressures in region *D* become dominant. For stronger interactions, significant unsteadiness is observed in simulations [35] due to intermittent flow separation, and this can be the underlying cause of increasing pressure fluctuations in region *D*.

Correlation maps of the 8° and 10°DF cases are compared in Fig. 14. When the reference point (star in green) is chosen near the shock-crossing (first row in Fig. 14), both 8°DF and 10°DF show highly correlated fluctuations with the upstream ($0 < x/\delta < 8$), seen as red and blue bands in the middle of the interaction. For 10°DF, the stronger case, the high correlation regions span the entire middle region between the fins. In contrast, the spanwise extent for 8°DF, the weaker case, is much smaller. When the reference point is located on the oblique shock closer to the fin in the quasi-conical region (second row in Fig. 14), correlation region of 8°DF looks more similar to the 10°SF case (see Fig. 7a) rather than the 10°DF case. This is consistent with the fact that the quasi-conical region is larger for the weaker case where the disturbances are convected away from the interaction origin (near the fin tip) along interaction rays (i.e., less influenced by the unsteadiness in region *D* in Fig. 13a), while the stronger interaction is largely dominated by the dynamics near the centerline. Lastly, moving the reference point closer to the fin near the interior Kulite (third row in Fig. 14) shows that for the weaker interaction the correlation pattern is more localized and correlation with upstream is insignificant.

As can be deducted from the discussion so far, centerline is an important point of reference for DF interactions. Figure 15 compares the centerline spectrogram for 8° and 10°DF. Similar to the 10°DF, recalling the discussion for Fig. 8b in Sec. III.A.3, 8°DF case also shows low-frequency unsteadiness near the upstream influence but with a lower magnitude than 10°DF. The existence of low-frequency unsteadiness on a DF configuration for a stronger interaction is attributed to a compound 3-D closed separation [35]. Even though there exists no separation along the vicinity of the

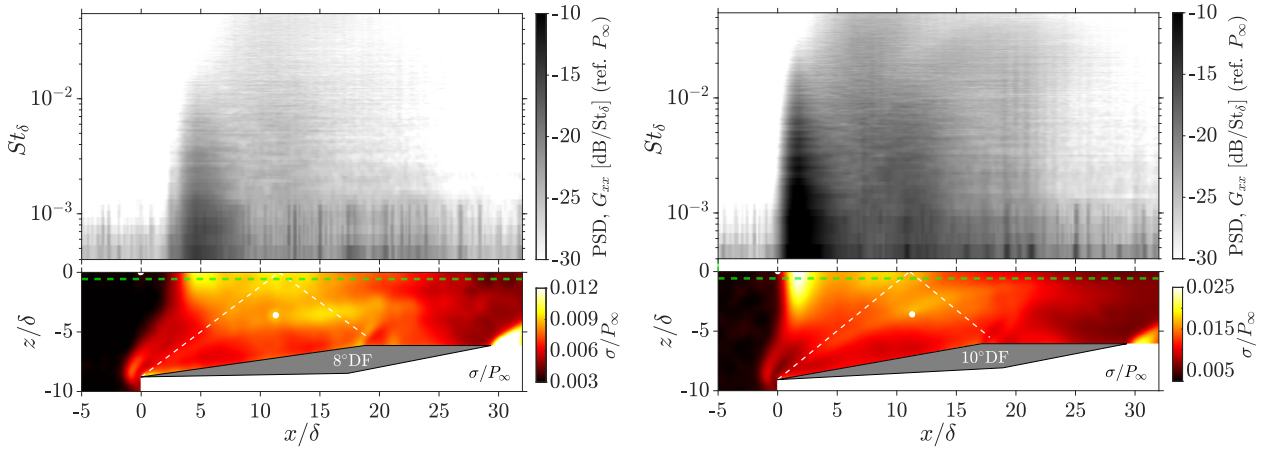

(a) 8° Double-Fin **(b) 10° Double-Fin**

Fig. 15 Comparison of near-centerline Power Spectral Density (PSD) between 8°DF and 10°DF. Obtained from unsteady PSP. Green-dashed lines plotted on the standard deviation field (bottom) show the location where the PSD field (top) is extracted from. White dashed lines indicate inviscid oblique shocks.

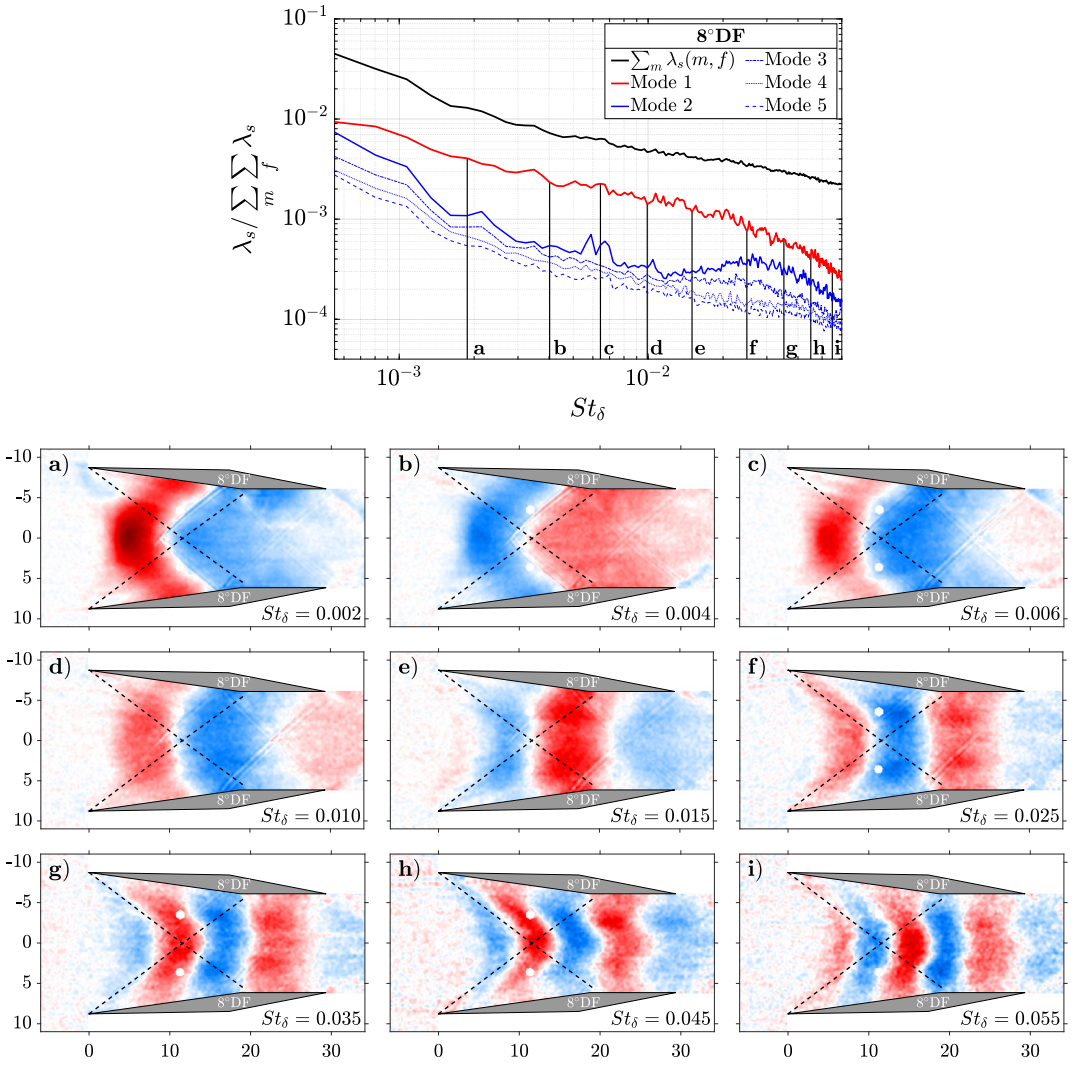

Fig. 16 Normalized eigenvalue spectra and the real part of the first mode of SPOD extracted from unsteady PSP at various frequencies for 8° Double-Fin. Red and blue color scales are symmetric and arbitrary, and white color represents zero. Mode shapes are animated in the Supplementary Video S7. Black dashed lines indicate inviscid oblique shocks.

centerline, the results clearly show that in the vicinity of UI, the interaction exhibits low-frequency unsteadiness and it is more pronounced as the interaction strength increases.

The normalized eigenvalue spectra of the first five SPOD modes out of a total of 50 modes, along with the mode shapes of the real part of the first mode at selected frequencies, are shown in Fig. 16 for 8°DF (see Supplementary Video S7). The eigenvalue spectra of 8°DF looks very similar to 10°DF (see Fig. 10), which monotonically decreases with increasing frequency. All the mode shapes for 8°DF show features that are similar to the stronger 10°DF case. The origin of the traveling pressure waves appears to be near the UI, as discussed before (see the discussion of Figs. 9 and 10 in Sec. III.A.3), which coincides with region *D* in Fig. 13a. This suggests that the region *D*, an interaction area with one of the highest levels of unsteady pressure loads is the source of these energetic pressure waves that propagate

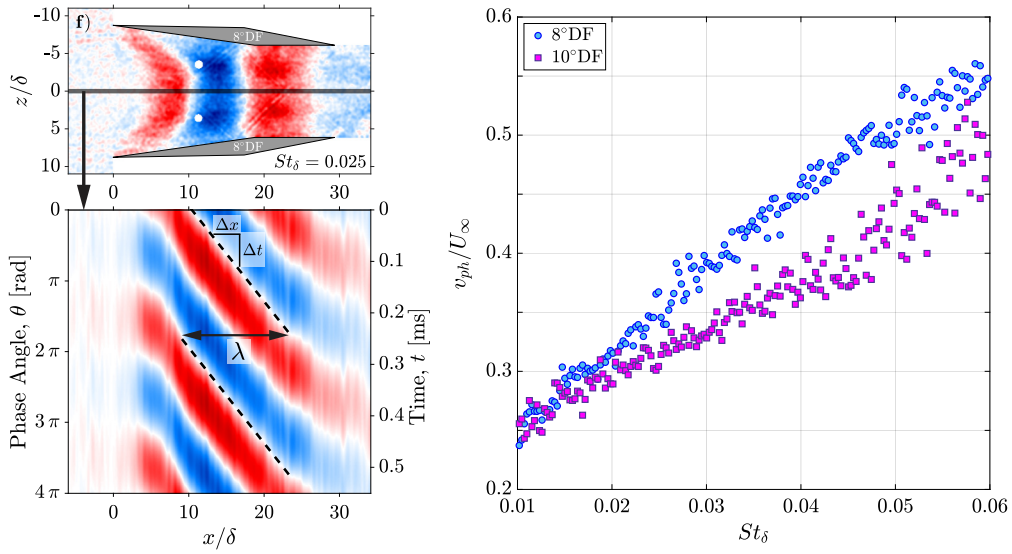

(a) Wave diagram **(b) Phase velocity distribution for $10 < x/\delta < 21$**

Fig. 17 A representative mode shape from 8° Double-Fin SPOD (top-left) and its wave diagram (bottom-left); waves are extracted from the mode shape centerline and ordered in successive phase ($\theta = 2\pi f t$). Phase velocity ($v_{ph} = \lambda f \approx \Delta x/\Delta t$, obtained from wave diagrams) distribution against Strouhal number ($St_\delta = f\delta/U_\infty$) (right).

downstream.

C. Characteristics of Surface Pressure Waves

As high energy mode shapes are often considered a signature of energetic structures, further examination of these traveling waves is warranted. In Fig. 17, we depict the behavior of these waves. A representative mode shape from 8°DF ($St_\delta = 0.025$) and its wave diagram are shown in Fig. 17a. As seen here, the centerline data is extracted from the SPOD mode shape (top-left). This mode is advanced in time by multiplying the mode shape with $e^{i\theta}$, where the phase angle ($\theta = 2\pi f t$) contains the time t and frequency f information; the frequency is already embedded within the selected Strouhal number ($St_\delta = f\delta/U_\infty$). Thus, a wave diagram is constructed where the x-axis is x/δ and the y-axis is the phase angle of the centerline mode shape (bottom-left). In the wave diagram, a region of quasi-parallel straight zero-crossings (i.e., the amplitude of the wave is zero somewhere between the crest and the trough along the x-axis) is clearly visible, where two dashed black lines are added for clarity. The horizontal spacing between these lines represents a good approximation of the wavelength λ, where the phase velocity of the wave ($v_{ph} = \lambda f \approx \Delta x/\Delta t$) is nearly constant. When the same approach is applied to other mode shapes at different frequencies in $10 < x/\delta < 21$ where it corresponds roughly to the region between the shock-crossing and the centerline interaction of expansion fans, the normalized phase velocity (v_{ph}/U_∞) distribution is obtained as a function of Strouhal number (St_δ) as depicted in Fig. 17b. Both the 8°DF and 10°DF cases show similar trend, that is, the phase velocity increases with increasing frequency. In the wave diagram (Fig. 17a), it should be noted that the phase velocity of the waves near the UI before the

shock-crossing (roughly $4 < x/\delta < 7$, which corresponds underneath the λ-shock) are larger (the slope of zero-crossings are less steep) compared to the region of interest ($10 < x/\delta < 21$). Considering the intermittent behavior of the front-foot of the λ-shock, strong pressure fluctuations are introduced on the surface starting at the UI due to the unsteady back and forth movement of the front-foot. The phase velocity of these pressure disturbances underneath the λ-shock decreases after the shock-crossing (rear-foot to be more specific). This decrease in the phase velocity shows the same decreasing trend with the velocity flowfield above the surface; velocity of the flow decreases while crossing a shock wave (i.e., rear-foot of the crossing shock). Similarly, when compared to the region of interest, the phase velocity of the waves also increases in the region after the expansion fans start crossing in the centerline (roughly $x/d > 24$). Since expansion fans accelerate the incoming flow, the increase in the phase velocities again shows a similar trend with the increasing flow velocities above the surface. Note that the fading colors observed in this region ($x/d > 24$) indicate a decrease in pressure fluctuation as the flow passes through the expansion fan interaction region. Moreover, phase velocities of 8°DF are larger overall than 10°DF case. This can be explained from the observation that the phase velocities of the pressure waves show similar behavior with the flow velocities above the surface. Since the strength of the shocks (i.e., M_n) produced by the 8°DF is less when compared to the 10°DF, velocities in the flowfield above the surface behind the shocks are faster in the 8°DF case, resulting in higher phase velocities for 8°DF.

To better understand the relation between the frequency and wavenumber ($k = 2\pi/\lambda$), the wave dispersion relation along the interaction centerline is plotted in Fig. 18a-b, in which the phase velocity ($v_{ph} = 2\pi f/k = 2\pi U_\infty St_\delta/k\delta$) data from Fig. 17b is replotted. The gray scale spectrogram in Fig. 18 is the 2-D space-time Fourier transform on the mean-subtracted normalized pressure field (P/P_∞ obtained from unsteady PSP) along the centerline; a Fourier transform in x-axis is utilized with zero padding to increase the resolution in wavenumber domain by tenfold, followed by the PSD calculation in time-axis by using Welch's method of periodograms [47]. The green-dots show the peak points of the space-time spectrogram, and the white-dashed line represents a linear curve fit for the peak points in $0.02 < St_\delta < 0.06$. As seen here, the dispersion relation obtained from SPOD modes agrees reasonably well with the trend in the space-time Fourier transform analysis for both 8°DF and 10°DF. However, results from SPOD modes predicts slightly lower phase velocities compared to the peak points (green-dots) of the space-time spectrogram. This is expected since the dispersion relation estimation from SPOD only considers the region of interest ($10 < x/\delta < 21$), whereas the space-time Fourier transform is applied to the entire centerline ($-5 < x/\delta < 35$). Recalling the discussion where the phase velocity is found to be greater under the λ-shock and in the expansion fan interaction region when compared to the region of interest, the overall phase velocity can easily be anticipated to be larger than the phase velocities in the region of interest which causes the peak points to shift towards the lower wavenumbers as seen in Fig. 18a-b. Additionally, the same space-time Fourier transform analysis are repeated only including the region of interest, and the results are shown in Fig. 18c-d. As noticed, the results from SPOD are in good agreement with the space-time spectrogram. Furthermore, for $St_\delta < 0.01$, wavenumbers are spread into a broad range which is clearly seen with the dark region in Fig. 18b. This

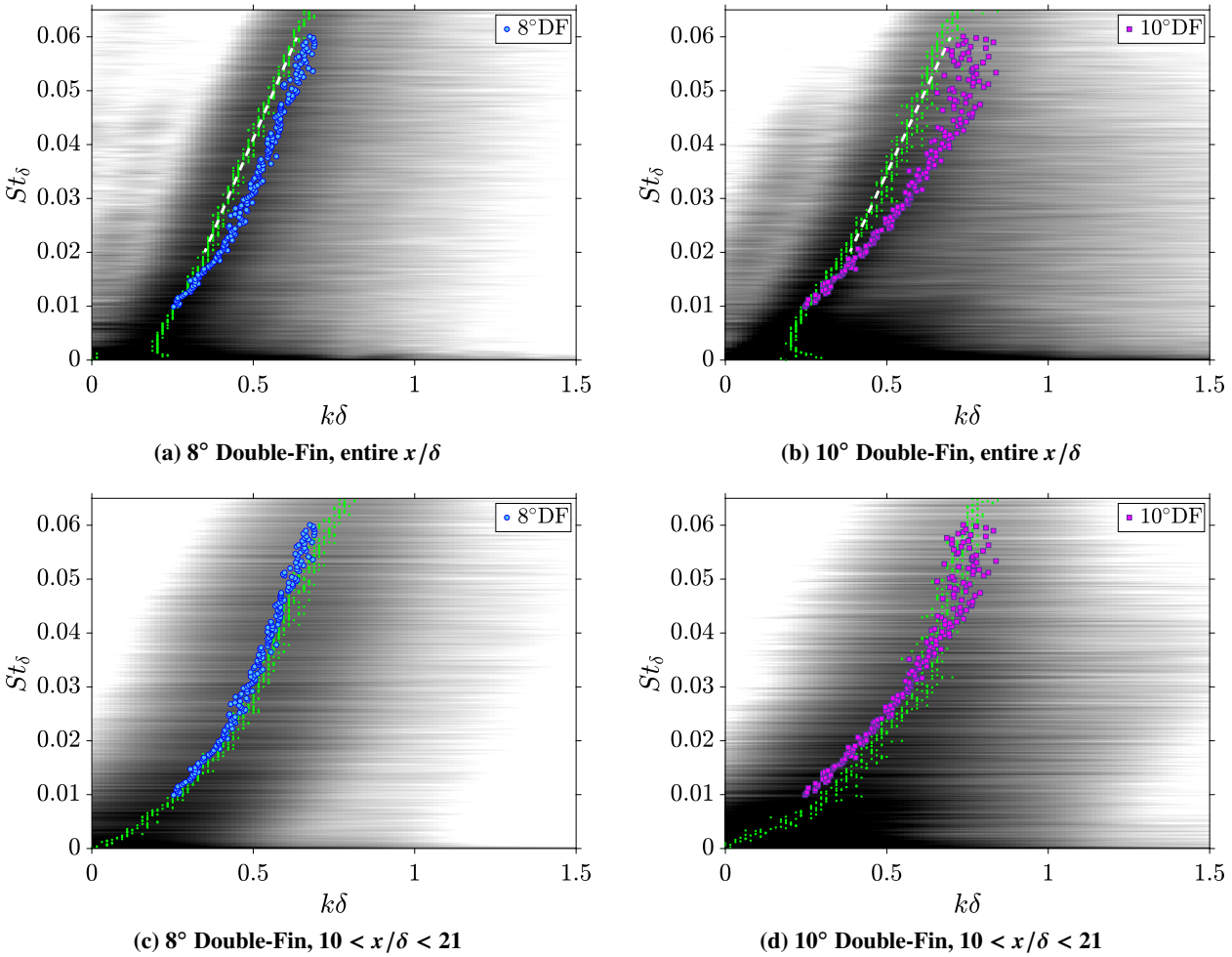

(a) 8° Double-Fin, entire x/δ

(b) 10° Double-Fin, entire x/δ

(c) 8° Double-Fin, $10 < x/\delta < 21$

(d) 10° Double-Fin, $10 < x/\delta < 21$

Fig. 18 Dispersion relation in the interaction centerline. Spectrogram of 2-D space-time Fourier transform of the mean-subtracted normalized pressure fluctuations (P/P_∞ obtained from unsteady PSP); markers of blue-circles (8°DF) and magenta-squares (10°DF) are equivalent to the phase velocity distributions in Fig. 17b. Green-dots indicate the peak points of the space-time spectrogram where the gray scale colormap is logarithmic.

is also evident in the mode shapes shown in Figs. 16 and 10 where the waves in the centerline is like a skewed sine wave. When the zero-crossing is taken as a reference, the upstream portion of these waves is significantly shorter than the downstream portion whereas the crest or trough location in the upstream portion is also distorted further upstream as seen in Fig. 10a-c. Therefore, it is not feasible to estimate a single distinct wavelength for such waves wherein the downstream tail of the wave also extends beyond the fin trailing edge.

The most salient result obtained from these diagrams demonstrates that the waves with larger wavenumbers (shorter wavelengths) travel with larger phase velocities. Phase velocity being dependent on wavenumber suggests these waves being dispersive, meaning due to different wavelengths traveling at different speeds, waves will disperse as they propagate downstream. The superposition of these waves containing a range of wavenumbers traveling with their own phase velocities disperses into an oscillatory wave train as time evolves, and the overall propagation of this group of

wavenumbers through this oscillatory wave train is the group velocity where the energy is also found to propagate with the group velocity [50]. The overall group velocity ($\upsilon_{gr} = 2\pi df/dk = 2\pi U_\infty dSt_\delta/dk\delta$) is proportional to the slope of the curve in Fig. 18a-b which is approximated as white-dashed line in the region between $0.02 < St_\delta < 0.06$ by using linear curve fitting over the peak points shown with green-dots. The overall normalized group velocities (υ_{gr}/U_∞) can be calculated as 0.88 and 0.81 for 8°DF and 10°DF, respectively, and the group velocities are larger than the phase velocity shown therein; meaning the energy contained in the pressure fluctuations travel faster than each phase velocity shown in these analysis. However, it should be noted that the straight line approximation (white-dashed line in Fig. 18a-b) does not well represent the dispersion relation when different regions of the interaction are considered as demonstrated previously. For instance, when the peak points of Fig. 18a-b is compared with Fig. 18c-d, it is clearly seen that a second (or higher) order curve fitting is more pertinent for the region $10 < x/\delta < 21$ in contrast to the entire centerline region, indicating an increase in the group velocity (steepening slope in Fig. 18c-d) as the frequency increases. Therefore, group velocities are expected to vary locally which also suggests dispersive behavior as far as the group velocity is concerned.

D. Centerline Mean Surface Pressure

The normal Mach number (M_n), which represents the strength of the interaction, as discussed earlier in Sec. III.B.2, along with the incoming boundary-layer thickness, forms the primary parameters that characterize a sufficiently tall SF (a semi-infinite) interaction. However, DF SBLI generates a different flow topology; flow features cannot be simply constructed with the superposition of two SF SBLI. Additional scaling parameters, such as the spacing between the two fin tips W, may come into play and their role should be explored, where possible.

The present study is limited to only two fin-tip-spacing conditions. To gain further insights into the role of fin-tip-spacing, a comparison is made with previous studies [21, 28]. Figure 19a depicts a comparison between the surface pressures along the centerline for 10°DF case and the DF interactions of similar strength (M_n) reported in Refs. [21, 28]. It is worth noting the freestream boundary-layer thicknesses of all the cases are also relatively similar, within 3.3-3.8 mm. For this comparison, we use a different frame of reference, where its origin is located at the shock-crossing ($x^* = 0$). As noted in the discussion of Fig. 12, the UI length is an important parameter in determining the interaction size for DF SBLI relative to the shock-crossing location. Figure 19a shows the centerline pressure distributions from different studies where the streamwise distance is normalized by the incoming boundary-layer thickness δ from the respective experiments. As seen, the UI locations (and lengths) are different between the studies. Given the similarity in interaction strengths and incoming boundary-layer thicknesses for these studies, the difference is likely attributed to another parameter — the fin-tip-spacing is a logical choice to examine. Since the interaction strengths (M_n) of all the cases are similar, the dependency of the UI length on M_n (see Sec. III.B.2) is marginal. When the differences in fin-tip-spacing are considered, it is expected that the UI length of the present study is significantly shorter than other cases. This difference arises because UI length increases as one moves away from the VCO due to the

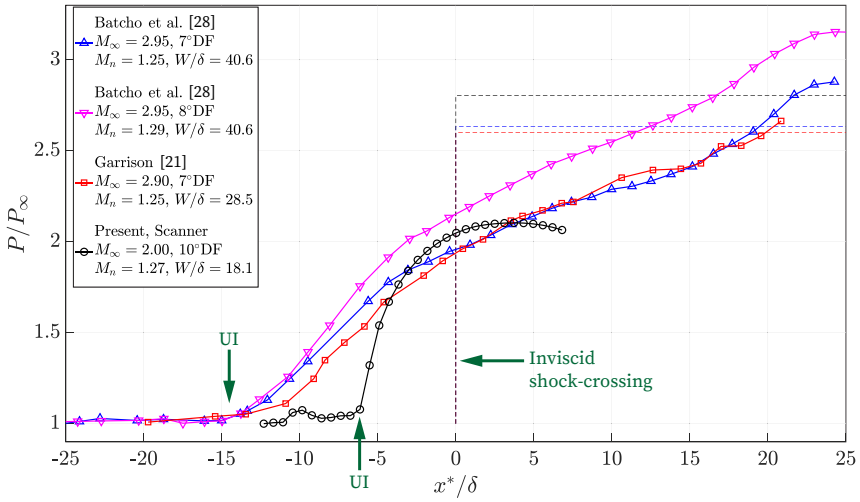

(a) Scaling with incoming boundary-layer thickness, δ.

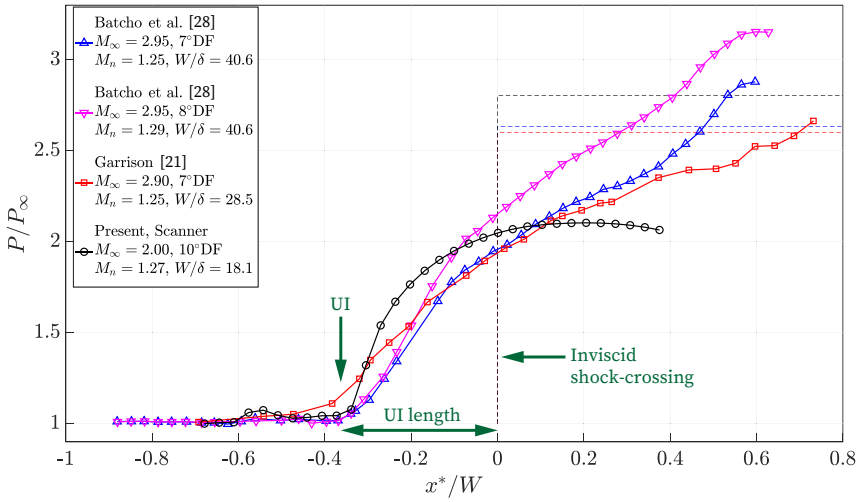

(b) Scaling with fin-tip-spacing, W.

Fig. 19 Comparison of scaling parameters using the centerline pressure measurements of the present 10° Double-Fin with the previous Double-Fin studies [21, 28] of similar interaction strength (based on M_n). Dashed lines show the pressure jump across an equivalent inviscid shock-crossing. UI: Upstream Influence.

nature of the quasi-conical symmetry, wherein the front-foot of the λ-shock grows further upstream from the inviscid shock location. Therefore, the distance from the symmetry plane to the fin-tip bounds the size of the λ-shock at the interaction centerline, meaning smaller fin-tip-spacing leads to a smaller UI length when the interaction strength is maintained constant. For this reason, the data sets in Fig. 19a are replotted by using the fin-tip-spacing W as the scaling parameter and the results are shown in Fig. 19b. Normalization with the corresponding fin-tip-spacing illustrates that all the cases show similar UI length where pressure starts to increase from freestream levels ($x^*/W \approx -0.35$). These analyses are based on comparisons with the available data for comparable DF interactions, which is fairly limited. While any generalizations need to be viewed cautiously, these results suggest that fin-tip-spacing is an important parameter

that warrants further exploration. Therefore, an additional parameter of δ/W should be considered in characterizing the upstream development of DF interactions.

IV. Conclusions

Experimental investigations of mean and unsteady surface flowfield characteristics of shock-wave/boundary-layer interaction on symmetric Double-Fin with 8° and 10° fin angles are performed at Mach 2. To examine global flow behavior and its characteristics, oil surface flow visualization and steady/unsteady PSP measurements are applied for both fin angle cases. The unsteady surface flow features are investigated through correlation analysis, standard deviation mapping, and SPOD by using unsteady PSP data. The details of DF SBLI are directly compared with SF SBLI for the 10° fin angle to provide unique insights into the distinct features of DF SBLI. Higher surface pressures are observed for DF SBLI compared to the corresponding SF SBLI since crossing of two shocks are involved in DF. Further, quasi-conical symmetry, a signature of SF SBLI, breaks as one approaches the centerline of DF SBLI. For SF, in particular, iso-pressure contours are roughly parallel to the quasi-conical interaction symmetry rays emanating from the VCO. In contrast, iso-pressure contours are oriented nearly orthogonal to the freestream in the interaction region for DF. In essence, the interaction region between the two fins begins to depict quasi 2-D behavior, especially in the areas close to the centerline. The effect of fin angle is evaluated by comparing interaction features of 8°DF and 10°DF. General flow features are shown to be similar for surface oil flow visualization and steady/unsteady PSP measurements for both cases, such as the existence of the CDC region and separation vortex. The stronger interaction (larger M_n) showed significantly higher pressure fluctuations wherein significant low-frequency unsteadiness is noticed for the DF cases. Traveling surface pressure waves are identified for a broad range of frequencies as a result of SPOD analysis. It is observed that these waves exhibit dispersive behavior and the wave generation occurs near the UI. Dispersion relation in the DF centerline is investigated through 2-D space-time Fourier transform of unsteady PSP and results are compared with the phase velocity analysis of the traveling waves obtained from SPOD. A remarkable overlap is identified between the two techniques wherein the phase and group velocity relations are examined for distinct regions of the interaction. Centerline pressure distribution of the present study is compared to previous studies with similar interaction strength and freestream boundary-layer thickness. Fin-tip-spacing is found to be an important normalization parameter for DF SBLI on determining the UI length.

Acknowledgments

This work was supported by the Florida Center for Advanced Aero-Propulsion (FCAAP) at FAMU-FSU College of Engineering, and Don Fuqua Eminent Scholar Fund. Additional support is provided by the Air Force Office of Scientific Research (AFOSR).

References

[1] Seçkin, S., Mears, L. J., Song, M., Zigunov, F., Sellappan, P., and Alvi, F. S., "Surface Properties of Double-Fin Generated Shock-Wave/Boundary-Layer Interactions," *AIAA Scitech 2022 Forum*, 2022, p. 0701. https://doi.org/10.2514/6.2022-0701.

[2] Babinsky, H., and Harvey, J. K., *Shock Wave-Boundary-Layer Interactions*, Cambridge Aerospace Series, Vol. 32, Cambridge University Press, 2011. https://doi.org/10.1017/CBO9780511842757.

[3] Dolling, D. S., "Fifty Years of Shock-Wave/Boundary-Layer Interaction Research: What Next?" *AIAA Journal*, Vol. 39, No. 8, 2001, pp. 1517–1531. https://doi.org/10.2514/2.1476.

[4] Anderson Jr, J. D., *Hypersonic and High-Temperature Gas Dynamics*, American Institute of Aeronautics and Astronautics, 2006. https://doi.org/10.2514/4.105142.

[5] Zheltovodov, A. A., and Knight, D. D., "Ideal-Gas Shock Wave-Turbulent Boundary-Layer Interactions in Supersonic Flows and Their Modeling: Three-Dimensional Interactions," *Shock Wave-Boundary-Layer Interactions*, Cambridge Aerospace Series, Vol. 32, edited by H. Babinsky and J. K. Harvey, Cambridge University Press, 2011, pp. 202–258. https://doi.org/10.1017/CBO9780511842757.005.

[6] Gaitonde, D. V., "Progress in shock wave/boundary layer interactions," *Progress in Aerospace Sciences*, Vol. 72, 2015, pp. 80–99. https://doi.org/10.1016/j.paerosci.2014.09.002.

[7] Délery, J., Marvin, J. G., and Reshotko, E., "Shock-Wave Boundary Layer Interactions," Tech. Rep. 280, Advisory Group for Aerospace Research and Development (AGARD), 1986.

[8] Settles, G. S., and Dolling, D. S., "Swept Shock Wave/Boundary Layer Interactions," *Tactical Missile Aerodynamics*, Progress in Astronautics and Aeronautics, Vol. 104, edited by M. J. Hemsch and J. N. Nielsen, American Institute of Aeronautics and Astronautics, 1986, pp. 297–379.

[9] Dolling, D. S., and Bogdonoff, S. M., "Upstream Influence in Sharp Fin-Induced Shock Wave Turbulent Boundary-Layer Interaction," *AIAA Journal*, Vol. 21, No. 1, 1983, pp. 143–145. https://doi.org/10.2514/3.8041.

[10] Alvi, F. S., and Settles, G. S., "Physical Model of the Swept Shock Wave/Boundary-Layer Interaction Flowfield," *AIAA Journal*, Vol. 30, No. 9, 1992, pp. 2252–2258. https://doi.org/10.2514/3.11212.

[11] Alvi, F. S., and Settles, G. S., "Structure of Swept Shock Wave/Boundary-Layer Interactions Using Conical Shadowgraphy," *21st Fluid Dynamics, Plasma Dynamics and Lasers Conference*, 1990, p. 1644. https://doi.org/10.2514/6.1990-1644.

[12] Arora, N., "Flowfield of a Three-Dimensional Swept-Shock Boundary Layer Interaction at Mach 2," Ph.D. thesis, The Florida State University, 2018. https://doi.org/10.13140/RG.2.2.24882.56001.

[13] Settles, G. S., and Lu, F. K., "Conical Similarity of Shock/Boundary-Layer Interactions Generated by Swept and Unswept Fins," *AIAA Journal*, Vol. 23, No. 7, 1985, pp. 1021–1027. https://doi.org/10.2514/3.9033.

[14] Knight, D. D., and Badekas, D., "On the Quasi-Conical Flowfield Structure of the Swept Shock Wave-Turbulent Boundary Layer Interaction," *22nd Fluid Dynamics, Plasma Dynamics and Lasers Conference*, 1991, p. 1759. https://doi.org/10.2514/6.1991-1759.

[15] Gaitonde, D. V., and Knight, D. D., "Numerical Experiments on the 3-D Shock Wave-Boundary Layer Interaction Generated by a Sharp Fin," *26th Aerospace Sciences Meeting*, 1988, p. 309. https://doi.org/10.2514/6.1988-309.

[16] Mears, L. J., Baldwin, A., Ali, M. Y., Kumar, R., and Alvi, F. S., "Spatially resolved mean and unsteady surface pressure in swept SBLI using PSP," *Experiments in Fluids*, Vol. 61, No. 4, 2020, pp. 1–14. https://doi.org/10.1007/s00348-020-2924-x.

[17] Mears, L. J., Sellappan, P., and Alvi, F. S., "Tomographic PIV in Fin-Generated Shock Wave/Boundary-Layer Interaction at Mach 2," *AIAA Scitech 2020 Forum*, 2020, p. 0584. https://doi.org/10.2514/6.2020-0584.

[18] Mears, L. J., Sellappan, P., and Alvi, F. S., "Three-Dimensional Flowfield in a Fin-Generated Shock Wave/Boundary-Layer Interaction Using Tomographic PIV," *AIAA Journal*, 2021, pp. 1–12. https://doi.org/10.2514/1.J060356.

[19] Alvi, F. S., "Flowfield Structure of Swept Shock Wave/Turbulent Boundary-Layer Interactions," Ph.D. thesis, The Pennsylvania State University, 1992.

[20] Tobak, M., and Peake, D. J., "Topology of Three-Dimensional Separated Flows," *Annual Review of Fluid Mechanics*, Vol. 14, No. 1, 1982, pp. 61–85. https://doi.org/10.1146/annurev.fl.14.010182.000425.

[21] Garrison, T. J., "The Interaction Between Crossing-Shock Waves and a Turbulent Boundary Layer," Ph.D. thesis, The Pennsylvania State University, 1994.

[22] Adler, M. C., and Gaitonde, D. V., "Flow Similarity in Strong Swept-Shock/Turbulent-Boundary-Layer Interactions," *AIAA Journal*, Vol. 57, No. 4, 2019, pp. 1579–1593. https://doi.org/10.2514/1.J057534.

[23] Adler, M. C., and Gaitonde, D. V., "Dynamics of Strong Swept-Shock/Turbulent-Boundary-Layer Interactions," *Journal of Fluid Mechanics*, Vol. 896, 2020. https://doi.org/10.1017/jfm.2020.334.

[24] Vanstone, L., Saleem, M., Seçkin, S., and Clemens, N. T., "Role of Boundary-Layer on Unsteadiness on a Mach 2 Swept-Ramp Shock/Boundary-Layer Interaction Using 50 kHz PIV," *55th AIAA Aerospace Sciences Meeting*, 2017, p. 0757. https://doi.org/10.2514/6.2017-0757.

[25] Mears, L. J., "Three-Dimensional Flowfield in a Swept Shock Wave/Boundary-Layer Interaction and Its Response to Pulsed Microjet Actuation," Ph.D. thesis, The Florida State University, 2020.

[26] Vanstone, L., Musta, M. N., Seçkin, S., and Clemens, N. T., "Experimental study of the mean structure and quasi-conical scaling of a swept-compression-ramp interaction at Mach 2," *Journal of Fluid Mechanics*, Vol. 841, 2018, pp. 1–27. https://doi.org/10.1017/jfm.2018.8.

[27] Mee, D. J., Stalker, R. J., and Stollery, J. L., "Glancing Interactions Between Single and Intersecting Oblique Shock Waves and a Turbulent Boundary Layer," *Journal of Fluid Mechanics*, Vol. 170, 1986, pp. 411–433. https://doi.org/10.1017/S0022112086000952.

[28] Batcho, P. F., Ketchum, A., Bogdonoff, S. M., and Fernando, E., "Preliminary Study of the Interactions Caused by Crossing Shock Waves and a Turbulent Boundary Layer," *27th Aerospace Sciences Meeting*, 1989, p. 359. https://doi.org/10.2514/6.1989-359.

[29] Poddar, K., and Bogdonoff, S. M., "A Study of the Unsteadiness of Crossing Shock Wave Turbulent Boundary Layer Interactions," *21st Fluid Dynamics, Plasma Dynamics and Lasers Conference*, 1990, p. 1456. https://doi.org/10.2514/6.1990-1456.

[30] Hingst, W. R., and Williams, K. E., "Interaction of Two Glancing, Crossing Shock Waves With a Turbulent Boundary-Layer at Various Mach Numbers," Tech. Rep. E-6566, NASA Technical Memorandum 103740, 1991.

[31] Garrison, T. J., and Settles, G. S., "Interaction Strength and Model Geometry Effects on the Structure of Crossing-Shock Wave/Turbulent Boundary-Layer Interactions," *31st Aerospace Sciences Meeting*, 1993, p. 780. https://doi.org/10.2514/6.1993-780.

[32] Garrison, T. J., Settles, G. S., Narayanswami, N., and Knight, D. D., "Structure of Crossing-Shock-Wave/Turbulent-Boundary-Layer Interactions," *AIAA Journal*, Vol. 31, No. 12, 1993, pp. 2204–2211. https://doi.org/10.2514/3.11916.

[33] Garrison, T. J., Settles, G. S., Narayanswami, N., and Knight, D. D., "Laser Interferometer Skin-Friction Measurements of Crossing-Shock-Wave/Turbulent-Boundary-Layer Interactions," *AIAA Journal*, Vol. 32, No. 6, 1994, pp. 1234–1241. https://doi.org/10.2514/3.12125.

[34] Garrison, T. J., Settles, G. S., Narayanswami, N., Knight, D. D., and Horstman, C. C., "Flowfield Surveys and Computations of a Crossing-Shock Wave/Boundary-Layer Interaction," *AIAA Journal*, Vol. 34, No. 1, 1996, pp. 50–56. https://doi.org/10.2514/3.13020.

[35] Adler, M. C., and Gaitonde, D. V., "Structure, Scale, and Dynamics of a Double-Fin Shock/Turbulent-Boundary-Layer Interaction at Mach 4," *AIAA Scitech 2019 Forum*, 2019, p. 0096. https://doi.org/10.2514/6.2019-0096.

[36] Arora, N., Ali, M. Y., Zhang, Y., and Alvi, F. S., "Flowfield measurements in a Mach 2 fin-generated shock/boundary-layer interaction," *AIAA Journal*, Vol. 56, No. 10, 2018, pp. 3963–3974. https://doi.org/10.2514/1.J056500.

[37] Liu, T., Sullivan, J. P., Asai, K., Klein, C., and Egami, Y., *Pressure and Temperature Sensitive Paints*, Vol. 1, Springer, 2005. https://doi.org/10.1007/978-3-030-68056-5.

[38] Gregory, J. W., Asai, K., Kameda, M., Liu, T., and Sullivan, J. P., "A review of pressure-sensitive paint for high-speed and unsteady aerodynamics," *Proceedings of the Institution of Mechanical Engineers, Part G: Journal of Aerospace Engineering*, Vol. 222, No. 2, 2008, pp. 249–290. https://doi.org/10.1243/09544100JAERO243.

[39] Bendat, J. S., and Piersol, A. G., *Random Data: Analysis and Measurement Procedures*, John Wiley & Sons, 2010. https://doi.org/10.1002/9781118032428.

[40] Sugimoto, T., Sugioka, Y., Numata, D., Nagai, H., and Asai, K., "Characterization of Frequency Response of Pressure-Sensitive Paints," *AIAA Journal*, Vol. 55, No. 4, 2017, pp. 1460–1464. https://doi.org/10.2514/1.J054985.

[41] Peng, D., Jensen, C. D., Juliano, T. J., Gregory, J. W., Crafton, J., Palluconi, S., and Liu, T., "Temperature-Compensated Fast Pressure-Sensitive Paint," *AIAA Journal*, Vol. 51, No. 10, 2013, pp. 2420–2431. https://doi.org/10.2514/1.J052318.

[42] Khalil, G. E., Costin, C., Crafton, J., Jones, G., Grenoble, S., Gouterman, M., Callis, J. B., and Dalton, L. R., "Dual-luminophor pressure-sensitive paint: I. Ratio of reference to sensor giving a small temperature dependency," *Sensors and Actuators B: Chemical*, Vol. 97, No. 1, 2004, pp. 13–21. https://doi.org/10.1016/S0925-4005(03)00484-2.

[43] Fang, S., "Application of Fast-Responding Pressure-Sensitive Paint to a Hemispherical Dome in Unsteady Transonic Flow," Master's thesis, The Ohio State University, 2010.

[44] Ishiguro, Y., Nagai, H., Asai, K., and Nakakita, K., "Visualization of Hypersonic Compression Corner Flows using Temperature-and Pressure-Sensitive Paints," *45th AIAA Aerospace Sciences Meeting and Exhibit*, 2007, p. 118. https://doi.org/doi.org/10.2514/6.2007-118.

[45] Zigunov, F., Sellappan, P., Alvi, F. S., Ozawa, Y., Saito, Y., Nonomura, T., and Asai, K., "Time-resolved particle image velocimetry and pressure sensitive paint measurements of afterbody flow dynamics," *Physical Review Fluids*, Vol. 7, No. 2, 2022, p. 024701. https://doi.org/10.1103/PhysRevFluids.7.024701.

[46] Adler, M. C., "On the Advancement of Phenomenological and Mechanistic Descriptions of Unsteadiness in Shock-Wave/Turbulent-Boundary-Layer Interactions," Ph.D. thesis, The Ohio State University, 2019.

[47] Welch, P. D., "The Use of Fast Fourier Transform for the Estimation of Power Spectra: A Method Based on Time Averaging Over Short, Modified Periodograms," *IEEE Transactions on Audio and Electroacoustics*, Vol. 15, No. 2, 1967, pp. 70–73. https://doi.org/10.1109/TAU.1967.1161901.

[48] Towne, A., Schmidt, O. T., and Colonius, T., "Spectral proper orthogonal decomposition and its relationship to dynamic mode decomposition and resolvent analysis," *Journal of Fluid Mechanics*, Vol. 847, 2018, pp. 821–867. https://doi.org/10.1017/jfm.2018.283.

[49] Schmidt, O. T., and Towne, A., "An Efficient Streaming Algorithm for Spectral Proper Orthogonal Decomposition," *Computer Physics Communications*, Vol. 237, 2019, pp. 98–109. https://doi.org/10.1016/j.cpc.2018.11.009.

[50] Whitham, G. B., *Linear and Nonlinear Waves*, John Wiley & Sons, 1999. https://doi.org/10.1002/9781118032954.